Glial control of sphingolipid levels sculpts diurnal remodeling of sleep circuitry

Authors:

John Vaughen[1,2], Emma Theisen[1], Irma Magaly Rivas-Sema[3], Andrew B. Berger[1], Ina Anreiter[1], Vera C. Mazurak[3], Richard J. Reimer[4], M. Thomas Clandinin[3], Thomas R. Clandinin[1,5,*]

Affiliations:

[1]Department of Neurobiology, Stanford University; Stanford CA, 94305, United States.

[2]Department of Developmental Biology, Stanford University; Stanford, CA, 94305, United States.

[3]Department of Agriculture, Food, and Nutritional Science, University of Alberta; Edmonton, T6G 2R3, Canada.

[4]Department of Neurology and Neurological Sciences, Stanford University; Stanford, CA, 94305, United States.

[5]Lead Contact

*Corresponding author. trc@stanford.edu

Summary:

Structural plasticity in the brain often necessitates dramatic remodeling of neuronal processes and attendant reorganization of both the cytoskeleton and plasma membrane. While cytoskeletal restructuring has been studied extensively, how changes in specific lipids might orchestrate structural plasticity remain incompletely understood. We show that specific glial cells in *Drosophila* produce Glucocerebrosidase (GBA) to locally catabolize sphingolipids, critical components of neuronal membranes. Defects in sphingolipid catabolism drive lysosomal dysfunction, causing *Gba1b* mutants to harbor protein aggregates that cycle across circadian time, are regulated by neural activity and the circadian clock, and plateau with age. Moreover, cell-specific perturbations reveal that sphingolipid catabolism is necessary for neurites in sleep circuits to extend and retract across the day, and for sleep behavior. Critically, reprogramming the temporal pattern of GBA expression in sleep-circuit neurons is sufficient to invert the membrane remodeling cycle. Thus, dynamic changes in sphingolipid levels instruct the diurnal pattern of neuronal plasticity.

Keywords: structural plasticity; circadian; sleep; sphingolipids; glia; lysosomes; Glucocerebrosidase (GBA); proteostasis

Introduction

Lifelong brain function requires coordinated biosynthetic and degradative pathways to precisely maintain neural membrane composition, circuit function, and animal behavior. While protein synthesis and degradation have been studied extensively in neurons, our understanding of lipid metabolism in the brain is comparatively limited. Brains are lipid-rich and display regional heterogeneity in lipid species (O'Brien and Sampson, 1965)(Fitzner et al., 2020), which include the CNS-enriched sphingolipids (Merrill, 2011). Moreover, neurons can dynamically reshape their membranes as part of structural and synaptic plasticity. For example, sleep pacemaker neurons in both vertebrates and *Drosophila* undergo dramatic daily cycles of membrane addition and removal (Krzeptowski et al., 2018)(Becquet et al., 2008)(Fernández et al., 2008) that correlate with proper circadian cycles of behavioral activity (Petsakou et al., 2015). In addition, proteins that control membrane lipid composition are associated with Parkinson's Disease and Alzheimer's Disease (Yadav and Tiwari, 2014)(Lin et al., 2019) (Futerman and van Meer, 2004), and sleep and circadian dysfunction are common facets of neurodegeneration that can precede disease onset (Leng et al., 2019). However, surprisingly little is known about how specific lipid species are coupled to structural plasticity in neuronal membranes.

A prominent class of neural membrane lipids are the glycosphingolipids, which are built upon a core of Glucosylceramide (GlcCer) from the sphingolipid Ceramide (Cer). GlcCer is degraded by Glucocerebrosidase (GBA) (Figure 1A), and mutations in *GBA* are linked to sleep disruption and neurodegeneration. Complete loss of GBA activity invariably causes neuropathic Gaucher disease, and *GBA* carriers are ~3-5 times more likely to develop Parkinson's disease (Sidransky and Lopez, 2012) characterized by accelerated cognitive decline (Sidransky et al., 2009) (Liu et al., 2016). Mutations in *GBA* are also associated with isolated REM sleep behavior disorder (Gan-Or et al., 2015)(Krohn et al., 2020). However, the cellular mechanisms underpinning how mutations in *GBA* cause sleep and brain defects are unclear.

Drosophila is a powerful model for understanding GBA function: mutations in fly *gba1b* have evolutionarily conserved phenotypes, including lysosomal impairment, insoluble ubiquitin (Ubi) protein aggregates, and reduced sleep (Davis et al., 2016)(Kinghorn et al., 2016)(Kawasaki et al., 2017). Moreover, core sphingolipid regulatory enzymes (centered around Cer) are conserved in *Drosophila*, and mutations in these genes can cause neurodegenerative and behavioral changes (Acharya and Acharya, 2005) (Dasgupta et al., 2009)(Acharya et al., 2003). While prior studies identified a role for Gba1b in circulating extracellular vesicles (Jewett et al., 2021), the cellular requirements for Gba1b and GlcCer in the brain remain unknown, and evidence for how sphingolipids might shape neural circuitry and behavior is lacking *in vivo*.

We discover that *Drosophila* glia produce Gba1b to control lysosome homeostasis and sphingolipid degradation in adult neurons. Removal of *gba1b* from specific glial types triggered Ubi aggregates in both neurons and glia. Glia in both flies and humans have broadly conserved functions in neurotransmitter recycling, metabolism, and membrane phagocytosis (Freeman, 2015)(Yildirim et al., 2019). We identify neuropil ensheathing glia (EG), a glial type that is closely associated with neurites, as key mediators of sphingolipid catabolism. Remarkably, Ubi aggregates in young *gba1b* mutants shrink during the day and grow larger at night. This cycle of aggregate burden was modulated by the circadian clock and neural activity, as disrupting the circadian clock blocked aggregate cycling across the brain, and dark-rearing suppressed aggregate formation in the visual system. Moreover, glial sphingolipid catabolism is required to sustain cycles of neurite growth and retraction in sLNv neurons, which drive circadian rhythms and normal sleep patterns. Strikingly, reprogramming the temporal pattern of Gba1b by imposing

elevated expression of Gba1b at night in these neurons was sufficient to invert the normal cycle of neurite remodeling, with increased terminal volume at dusk instead of dawn. Thus, glia degradation of specific neuronal membrane sphingolipids is both necessary and sufficient to sculpt axon terminals across the day to maintain sleep and proteostasis.

Results

Gba1b is required in glia for lysosome function

To better characterize brain sphingolipid catabolism and Gba1b function, we generated an early frameshift allele, *gba1b*$^{\Delta 1}$, which we used in *trans* to *gba1b*$^{\Delta TT}$, a characterized null allele that also deletes an adjacent gene (Figure S1A, Table S1, (Davis et al., 2016)). We used transheterozygous combinations of these alleles to produce viable adults, designated *gba1b*$^{\Delta}$. Consistent with previous work (Kinghorn et al., 2016), we confirmed that *gba1b*$^{\Delta}$ brains harbor enlarged degradative lysosomes marked by an acidic-compartment label (LysoTracker), active proteases (Cathepsin B), and a lysosomal protein (Lamp) (Figure 1B-B'', Figure S1E-J), a phenotype detectable immediately after adult emergence. Aberrant lysosomes were distributed across the cortex of the brain and found within neurons (Figure S1K-N). We exploited this robust neuronal phenotype to identify where Gba1b is required for lysosome maintenance. Unexpectedly, *gba1b* knockdown (*RNAi*) or knockout (somatic *CRISPR*, *gba1b*^{cKO}) in all brain neurons did not cause any discernible lysosomal phenotypes (Figure 1C', D'). In contrast, pan-glial *gba1b* knockdown or knockout triggered lysosomal hypertrophy (Figure 1C'', D''). These data argue that neuronal lysosome function depends on Gba1b expression in glia.

We next attempted to rescue the *gba1b* LysoTracker phenotype using three Gba1b overexpression constructs (Table S2, Figure S1A): a wild-type *Gba1b* transgene, a catalytically-inactivate transgene (*Gba1b*^{E340K}), and a tethered *Gba1b*^{Lamp} transgene designed to restrict Gba1b to the lysosome and prevent Gba1b secretion (Mikulka et al., 2020). However, overexpressing Gba1b in neurons caused lysosomal hypertrophy in wild-type animals, a phenotype not seen upon overexpressing *Gba1b*^{E340K} (Figure S1O-P); strong induction of certain Gba1b transgenes in neurons also caused lethality or subviability (Table S2). Thus, excess Gba1b activity in neurons is detrimental to lysosomal homeostasis. To temper Gba1b induction in neurons, we placed Gba1b under the direct control of a neuronal enhancer (*nSyb::Gba1b*). *nSyb::Gba1b* produced lower Gba1b protein expression compared to overexpression constructs (Figure S1B-D). Interestingly, *nSyb::Gba1b* fully rescued the lysosomal phenotypes of *gba1b*$^{\Delta}$ mutants (Figure 1E'). Similarly, glial overexpression of *Gba1b*^{Lamp} or wild-type *Gba1b* also rescued the LysoTracker phenotype (Figure 1E'', Figure S1Q). Thus, while Gba1b is selectively produced by glia and sufficient to rescue *gba1b*$^{\Delta}$ mutant lysosomes, neurons can also utilize Gba1b for maintaining lysosome function.

We next tested if Gba1b was required in glia for other *gba1b*$^{\Delta}$ phenotypes. A hallmark of *gba1b*$^{\Delta}$ brains is progressive accumulation of insoluble, polyubiquitinated proteins (Kinghorn et al., 2016)(Davis et al., 2016). We found that older *gba1b*$^{\Delta}$ mutants accumulated Ubiquitin (Ubi) aggregates most prominently in both the inner optic lobe chiasm (OL-iCh) and in the Mushroom Body calyx cortex (MB-ca) (Figure 1G, Figure S2A-H). Ubi extensively colocalized with p62, which is an adaptor protein bridging Ubi and lysosomes and a common component of Ubi aggregates in fly and human neurodegeneration models (Bartlett et al., 2011) (Figure S2D-E). By expressing *p62-GFP* within neurons or glia in *gba1b*$^{\Delta}$ brains, we determined that MB-ca puncta were neural, whereas larger Ubi aggregates were glial, including OL-iCh aggregates (Figure S2

I-J). Similar to the LysoTracker phenotype, glial knockdown or knockout of *gba1b* induced Ubi aggregates, while neuronal perturbations did not (Figure 1H-I, Figure S2H). Conversely, glia expression of $Gba1b^{Lamp}$ in $gba1b^{\Delta}$ fully rescued both Ubi aggregate populations (Figure 1J and Figure S1R-S). *nSyb::Gba1b* also rescued neuronal MB-ca aggregates (Figure S1S-U) and surprisingly also rescued glial OL-iCh aggregates (Figure 1J'), but still harbored Ubi aggregates in barrier PNG glia (Figure S1U'). Taken together, Gba1b expression is required in glia to prevent lysosome dysfunction in neurons and subsequent Ubi aggregate appearance in both neurons and glia. However, Gba1b expression in neurons suffices to rescue $gba1b^{\Delta}$ aggregate formation in both neurons and subtypes of glia.

Specific glial subtypes are necessary and sufficient for Gba1b function in the brain

To identify which cells express Gba1b for brain proteostasis, we characterized $Gba1b^{GAL4}$, a gene trap in the Gba1b locus (Lee et al., 2018). $Gba1b^{GAL4}$ drove expression of a fluorescent reporter in glia (repo+ cells) but never in neurons (elav+ cells, Figure S3A-C). Combining $Gba1b^{GAL4}$ with a panel of *LexA*-based markers of individual glial types (Pfeiffer et al., 2008)(Kremer et al., 2017) revealed expression of Gba1b in neuropil ensheathing (EG), perineural (PNG), cortical, subperineural, and chiasm glia, but not astrocyte-like glia (Figure S3D-K). These data are consistent with a single-cell RNA-sequencing dataset (Davie et al., 2018). We next removed Gba1b from individual glia subtypes but found no LysoTracker phenotypes (Figure 2A, Figure S3L-M). However, given that $Gba1b^{GAL4}$ is expressed by multiple glia types, we reasoned that Gba1b may be redundantly produced for brain proteostasis. We therefore screened combinations of glial cell *gba1b* knockouts and found that removing Gba1b from both neuropil ensheathing glia (EG) and perineural (PNG) barrier glia caused lysosomal enlargement (Figure 2A''). $gba1b^{cKO}$ in EG and PNG also caused Ubi aggregate accumulation in the OL-iCh and the MB-ca (Figure 2B-C). Conversely, expression of wild-type *Gba1b* but not catalytically inactive $Gba1b^{E340K}$ in EG was sufficient to rescue the lysosomal and Ubi aggregate phenotypes seen in $gba1b^{\Delta}$ (Figure 2D-F). However, expression of wild-type Gba1b in PNG failed to rescue these phenotypes (Figure 2D'''-F'''), and expression of Gba1b in astrocytes (which extensively tile the synaptic neuropil) failed to rescue LysoTracker (Figure S3N, quantified in Figure 2G'). Importantly, EG, PNG, and astrocyte genetic drivers expressed high Gba1b protein selectively in each respective cell type (Figure S3O-Q). These data show that Gba1b is required in a cell-type specific manner to control neural lysosomes and protein aggregates, and hint at exclusive coupling between EG and neurons. Consistent with a critical role for Gba1b in EG, labeling EG membranes in $gba1b^{\Delta}$ revealed that Ubi aggregates in the OL-iCh and MB-ca were closely apposed to EG cells (Figure 2H-I). Thus, Gba1b is required in EG and PNG, and expression in EG is sufficient to rescue neuropil and cortex phenotypes.

Ubiquitin aggregates cyclically grow and shrink at younger ages

We next examined the onset of Ubi aggregate deposition in young $gba1b^{\Delta}$ flies and found an unanticipated relationship between aggregate burden and circadian time. Specifically, Ubi aggregates in the OL-iCh and the MB-ca were low or absent during the day but accumulated at night in 7-day old *gba1b* mutants (Figure 3A-F). We more closely examined the relationship between aggregates, age, and circadian zeitgeber time (ZT) entrained by 12 hour light/dark (LD) cycles. For both $gba1b^{\Delta}$ and glial $gba1b^{cKO}$ animals, a nadir of aggregate burden occurred at ZT6 (afternoon), and aggregates grew steadily through ZT12 (evening) and ZT18 (night) in the OL-

iCh (Figure 3G-L). Similarly, Ubi aggregates in the MB-ca were smaller during the day and larger at night in young flies (Figure S4A-D). However, in older flies, the difference between these timepoints was less pronounced (Figure 3H, J), arguing that aggregate clearance diminishes with age. In contrast to Ubi aggregates, lysosome markers were not as dramatically modulated by the circadian clock in *gba1b*$^{\Delta}$ null animals (Figure S4E-G). Subtle changes in control lysosome morphology were detected across ZT, consistent with circadian control of autophagosome production (Bedont et al., 2021)(Figure S4H-J). Thus, Ubi aggregates but not lysosomes undergo significant variations in size in *gba1b* mutants that tracked with fly circadian time.

Ubiquitin aggregate size is controlled by neural activity and the circadian clock

We hypothesized that the aggregate cycle apparent in *gba1b*$^{\Delta}$ flies could be directly controlled by the endogenous circadian clock, by light-evoked changes in neural activity (which entrains the clock), or by both. We tested these possibilities by depriving flies of light and by mutating *period* (*per*), a core component of the circadian clock (Figure 4A). Dark-rearing *gba1b*$^{\Delta}$ flies (DD) dramatically suppressed the number of Ubi aggregates in the OL-iCh, even in 20 day-old flies (Figure 4B, D). In contrast, Ubi aggregates in the MB-ca persisted in DD conditions (Figure 4C, E). This suggests that Ubi aggregates in the OL-iCh are sensitive to light and subsequent neural activity. In contrast, Ubi aggregates in the MB-ca are not responsive to light deprivation, perhaps because light does not strongly modulate neural activity in this region.

To test whether aggregate formation is under direct control of the endogenous circadian clock without the confound of light sensitivity, we focused on aggregate formation in the MB-ca. We entrained flies in LD, shifted to constant darkness for one day, and still detected lower aggregate burden at circadian time CT6 (Figure 4F-G). Moreover, introducing the arrhythmic *per*^{01} allele (Konopka and Benzer, 1971) into the *gba1b*$^{\Delta}$ background abolished cyclic changes in Ubi aggregate burden (Figure 4H-J). While mutating the circadian clock alone did not cause Ubi aggregates to accumulate in the OL-iCh (Figure S4K-N), we found enhanced Ubi burden in PNG and OL-iCh glia in *per*^{01}*; gba1b*$^{\Delta}$ flies (Figure S4O-P). Thus, neuronal aggregate size in the MB-ca is directly controlled by the circadian clock, and glial aggregate size in the OL-iCh is controlled by both neural activity and the circadian clock.

Specific sphingolipids accumulate in gba1b$^{\Delta}$ *brains*

As Gba1b degrades the lipid GlcCer, we next tested whether lipids were differentially controlled by Gba1b across circadian time. We dissected *gba1b*$^{\Delta}$ and control brains at 3 and 10 days, extracted lipids, and analyzed sphingolipids and phospholipids by liquid chromatography/mass spectrometry (Figure 5A). While bulk concentrations of phospholipids were unchanged (Figure S5A), the Gba1b substrate Glucosylceramide (GlcCer) was markedly increased across all *gba1b*$^{\Delta}$ samples, with high abundance at day 3 and higher amounts by day 10 (Figure 5B). Ceramide (Cer) was also stably increased in *gba1b*$^{\Delta}$ brains (Figure 5B'), which was previously observed in whole fly *gba1b* lipidomics (Jewett et al, 2021). In contrast, the most prevalent sphingolipid, Ceramide Phosphatidylethanolamine (CerPE), was unchanged (Figure 5B''). Removing *gba1b* in glia triggered a similar pattern of accumulation of GlcCer and Cer, while neuronal *gba1b* perturbation had no effect (Figure S5B). We further examined GlcCer localization using an antibody directed against GlcCer alongside neutral lipids using the lipophilic Nile Red stain. Both GlcCer and Nile Red were increased in *gba1b*$^{\Delta}$ brains compared to control animals (Figure 5C-D). Ectopic Nile Red-positive lipids in *gba1b*$^{\Delta}$ co-localized with

LysoTracker (Figure 5E) and also colocalized with GlcCer (Figure 5F). Thus, GlcCer accumulation in *gba1b*$^{\Delta}$ mutants localizes to engorged, lipid-filled lysosomes, and glial Gba1b is required to prevent GlcCer and Cer accumulation.

We more closely examined whether Gba1b controlled specific subsets of sphingolipids. Sphingolipids are classified by carbon chain length and the number of carbon-carbon double bonds on both the sphingoid base and fatty-acyl chain. In fly brains, we were able to detect ~50 GlcCer, ~50 Cer, and ~20 CerPE species (Table S3). Largescale changes in total brain Cer and GlcCer were driven by 6 of these species: d14:1/18:0, d14:1/20:0, d14:1/22:0, d16:1/18:0, d16:1/20:0, and d16:1/22:0. Together, these six species accounted for 80-87% of total GlcCer and 62-80% of total Cer by weight, and were also the main species detected in a *Saposin* lysosomal storage disorder model (Table S3; (Sellin et al., 2017)). Interestingly, while most examined GlcCer species were increased in *gba1b*$^{\Delta}$ brains (Figure S5C), a few rarer species, including GlcCer d15:0/22:1, were unchanged (Figure 5E). In contrast, dihydroceramide and diunsaturated Cer were largely unaffected in *gba1b* mutants (Figure S5D), as were CerPE subspecies (data not shown). Thus, glial Gba1b selectively catabolizes a subset of brain sphingolipids.

Sphingolipid catabolism is required for adult sleep behavior

As *gba1b*$^{\Delta}$ mutants have impaired lipid turnover and circadian-controlled aggregates, we reasoned that *gba1b* mutants might display defects in circadian neural circuits that rely on dynamic membrane remodeling. sLNv peptidergic neurons, which autonomously express pigment-dispersing factor (PDF), undergo dramatic daily remodeling of neurites and terminals (Fernández et al., 2008). This remodeling process and distribution of PDF is essential for the proper regulation of sleep and circadian patterns (Grima et al., 2004)(Parisky et al., 2008)(Choi et al., 2012) (Valadas et al., 2018). We therefore first tested whether *gba1b*$^{\Delta}$ mutants had deficiencies in circadian rhythms or sleep by measuring daily activity patterns. Control flies are crepuscular, with two bouts of activity surrounding dawn and dusk, with both sexes sleeping more at night than during the day (Figure 6A, (Helfrich-Förster, 2000)). Like controls, *gba1b* mutants began sleeping shortly after lights-off, but both sexes displayed diminished sleep during both day and night across the first 10 days of adult life (Figure 6A-B, Figure S6A). A similar suite of sleep deficits occurred in pan-glial knockout of *gba1b* (Figure 6C). Moreover, removing *gba1b* specifically in both EG and PNG also reduced sleep, especially in the daytime (Figure 6D). Depleting *gba1b* in solely EG did not cause obvious sleep defects, while depleting *gba1b* in PNG only reduced daytime sleep (Figure S6B), consistent with barrier glia regulating sleep (Artiushin et al., 2018). We also tested for persistence of circadian rhythms when *gba1b* mutants were moved to continuous darkness (DD) after entrainment in LD, and observed timely evening cessation of activity (Figure S6C-F). Together, these data argue that Gba1b function is required in specific glia for adult sleep behavior.

Sphingolipid levels drive cyclic remodeling of sLNv neurites

We hypothesized that the sleep deficit seen in *gba1b*$^{\Delta}$ mutants was caused by a failure to properly remodel sLNv neurites. In control animals, sLNv neurites are enlarged at dawn and smaller at dusk (Figure 7A; (Petsakou et al., 2015)). However, in *gba1b*$^{\Delta}$ mutants, sLNv neurites were trapped at an intermediate size in 5-day and 10-day old animals (Figure 7B, Figure S7A-B). Critically, knocking-out *gba1b* in EG and PNG also trapped sLNv neurites at a constant size

(Figure 7C, Figure S7C). Thus, *gba1b* is required non-autonomously in glia to remodel sleep circuitry. We next examined cell-type specific rescue of sLNv remodeling in *gba1b*$^{\Delta}$ mutants. Surprisingly, overexpressing Gba1b in EG failed to restore cyclic remodeling of sLNv terminals in *gba1b*$^{\Delta}$ mutants (Figure S7D), despite rescuing most lysosome and aggregate phenotypes (Figure 2). In contrast, *nSyb::Gba1b*, which expresses Gba1b pan-neuronally at lower levels, rescued sLNv remodeling in *gba1b*$^{\Delta}$ mutants (Figure 7D) in addition to histological defects (Figure 1). We infer that Gba1b can act directly in sLNv neurons and that remodeling may be sensitive to high levels of Gba1b expression in EG.

Given these observations, we hypothesized that the cycle of growth and retraction of sLNv terminals might reflect cyclic changes in the relative balance of sphingolipid biosynthesis and catabolism. If such cyclic changes play an instructive role in determining when sLNv neurons grow and shrink, altering the timing of Gba1b expression could alter the growth cycle. To do this, we took advantage of the Pdf promoter, which increases transcriptional expression in a narrow interval at dusk (Figure S7O) and produces elevated night and dawn PDF protein (Park et al., 2000). Strikingly, upon Gba1b induction in sLNv neurons with *Pdf-GAL4* in *gba1b*$^{\Delta}$ mutants, cyclic remodeling was rescued but occurred antiphase to wild-type controls, with larger neurite spread at dusk and reduced spread at dawn (Fig 7E). Importantly, *Gba1b*^{E340K} overexpression in sLNv neurons did not rescue the trapped sLNv neurites of *gba1b*$^{\Delta}$ mutants (Figure 7F). Notably, *Gba1b* expression in sLNv neurons did not rescue widespread histological phenotypes in *gba1b*$^{\Delta}$ mutants (Figure S7F-I), demonstrating that brain-wide lysotracker and protein aggregate are separable from sLNv remodeling. These data show that Gba1b activity is sufficient to directly control the temporal phase of sLNv membrane remodeling.

Given that Gba1b is normally not expressed in sLNv neurons but instead EG and other glia, we examined the spatial relationship between EG and sLNv neurites. We observed a striking physical association between EG and PDF protein localization, with EG membranes closely tracking PDF signal in sLNv neurites (Figure 7I-J, Figure S7J). Finally, we note that the PDF+ sLNv neurites in the MB-ca are associated with p62+ protein aggregates that cycle in *gba1b* mutants (Figure S7K-L). Taken together, our data show that Gba1b is required in glia that are closely associated with sLNv neurons to sustain the daily growth and retraction of neurites, and Gba1b activity in these neurites is sufficient to instruct a new rhythm of membrane remodeling.

Discussion

Our data demonstrate that glia produce Gba1b to non-autonomously control brain sphingolipids, protein degradation, and neurite remodeling in the sleep circuit (Figure 7K-N). We identified two specific glial subtypes, EG and PNG, as critical sources of Gba1b. EG are closely associated with remodeling neurites and selectively capable of rescuing neuronal lysosomes and protein aggregates in *gba1b* mutants. While previous genetic studies in vertebrate models did not determine whether GBA was required in glia or neurons (Enquist et al., 2007)(Keatinge et al., 2015)(Uemura et al., 2015), lysosomal GBA expression in mice and humans is ~5-fold higher in glia and microglia compared to neurons (Zhang et al., 2016)(Zhang et al., 2014), and *gba* mice harbor aggregates in astrocytes (Osellame et al., 2013). Given these expression patterns and the striking similarities in brain phenotypes seen across *GBA* mutants in flies, fish, and mammals, there appears to be an evolutionarily ancient role for glia in regulating sphingolipid metabolism in the brain.

glia locally sculpt neurites for temporally controlled circuit remodeling and behavior

Locally depleting *gba1b* in EG and PNG abrogated sLNv neurite remodeling, leaving a key circadian circuit locked into an intermediate state that correlated with sleep defects. Previous work identified the cytoskeletal effector Rho1 and the transcription factor Mef2 as important for sLNv neurite remodeling (Petsakou et al., 2015)(Sivachenko et al., 2013). Our work demonstrates that these changes must be coordinated with membrane remodeling, particularly sphingolipid degradation, and further shows that degradation is necessary for both membrane retraction and to sustain membrane growth. Critically, changing the timing of Gba1b expression in sLNv neurites inverted the circadian phase of sLNv remodeling, arguing for a casual role of sphingolipid levels in neurite remodeling.

Notably, the rate-limiting enzyme for *de novo* sphingolipid biosynthesis, *lace/SPT*, is bound by the transcription factor Clock (Abruzzi et al., 2011) and undergoes circadian changes in expression, peaking at midnight and potentially supplying sphingolipids for the dawn sLNv spread (Abruzzi et al., 2017)(Figure S7M). Egghead, which makes the glycosphingolipid MacCer from GlcCer, also cycles in LNv cells (Figure S7N). We propose that cyclical sphingolipid biosynthesis within sLNv neurons, combined with appropriate levels and timing of sphingolipid catabolism by Gba1b, determines the proper temporal phase of sLNv membrane remodeling (Figure 8). In this view, *gba1b* mutant animals break this cycle by impaired sphingolipid recycling, while expressing moderate levels of Gba1b under the control of the nSyb promoter sustains sLNv remodeling because the nSyb promoter affords appropriate levels and timing of Gba1b activity (and the nSyb promoter itself fluctuates over circadian time and is bound by Clock (Figure S7P; (Abruzzi et al., 2017)(Abruzzi et al., 2011)). Conversely, placing Gba1b under the control of a strong circadian promoter (Pdf, Figure S7O) drives premature processing of sphingolipids, causing the inverted neurite growth cycle (Figure 8).

In this model, it is tempting to speculate that the failure of high levels of Gba1b expression in the EG to rescue sLNv remodeling reflects the fact that these anomalously high expression levels might overwhelm sphingolipid biosynthesis pathways in sLNv neurons, locking them in a reduced state, a hypothesis consistent with the fact that Gba1b is normally expressed at extremely low levels in the adult brain (Davie et al, 2018) and that glial clocks are also required for sLNv remodeling (Herrero et al., 2017). Interestingly, blocking *de novo* sphingolipid synthesis in fibroblasts acutely reduced cell area and lamellipodia formation (Meivar-Levy et al., 1997), and altered sphingolipid profiles triggered shorter neurites and upregulation of RhoA following *acid ceramidase* knockdown in neuroblastoma lines. Moreover, *GBA2* (non-lysosomal) knockout mice have cytoskeletal defects (Raju et al., 2015), shorter neurites, and dysregulate Rho GTPase localization (Woeste et al., 2019). Taken with our work, sphingolipids and their regulatory enzymes may function “upstream” of Rho1 and cytoskeletal changes in sLNv remodeling, with more precise spatiotemporal control facilitated by glial degradation of remodeled neurites.

While sLNv neurites are a dramatic example of membrane remodeling, many neurons grow and shrink across circadian cycles and varied environmental conditions (Heisenberg et al., 1995)(Barth et al., 1997)(Pyza and Meinertzhagen, 1999). Membrane turnover is likely important during structural plasticity at synapses, and indeed *gba1b* flies have memory defects (Davis et al., 2016). As EG are broadly distributed throughout the brain (Kremer et al., 2017),

EG-mediated sphingolipid degradation may be central to membrane remodeling in many neural circuits. Interestingly, EG engulf neuronal membranes to clear damage in a sleep-dependent fashion (Doherty et al., 2009)(Musashe et al., 2016)(Stanhope et al., 2020), a cellular response potentially co-opted from a role in the daily remodeling of neurite membranes. Daily neurite remodeling is also a feature of the mouse suprachiasmatic nucleus (Becquet et al., 2008). Moreover, microglia, which express GBA in mice and humans, locally prune neurites during development and injury (Schafer et al., 2012)(Cangalaya et al., 2020), regulate sleep (Liu et al., 2021), and are enriched for sphingolipid catabolizing genes (Fitzner et al., 2020). Taken together, this suggests GBA could control many forms of structural plasticity across species.

Protein aggregation is dynamically controlled by circadian state and neural activity

Our characterization of *gba1b* mutant animals revealed a surprising circadian cycle of protein aggregate accumulation and removal in specific brain regions. Strikingly, we observed both activity-dependent and direct circadian control of aggregate burden. Protein aggregates have been described in wide-ranging models from flies to mice (Suresh et al., 2018) and are a prominent feature of neurodegeneration in humans (Ross and Poirier, 2004), including cells derived from *GBA* patients (Mazzulli et al., 2011)(Awad et al., 2015)(Schöndorf et al., 2014) and mice (Osellame et al., 2013). Given our observations, it may prove critical to characterize aggregate accumulation with respect to circadian time and neural activity. Indeed, circadian phagocytosis of amyloid-beta, a component of Alzheimer's aggregates, was recently observed in cultured macrophages and driven by circadian biosynthesis of heparan sulfate proteoglycans (Clark et al., 2022).

Lipids as linchpins of disease: a central role for glia and sleep

Our data provide a direct mechanistic connection between the enzymatic activity of Gba1b in glia to sleep behavior through sLNv neurite remodeling. Notably, *gba1b* mutant animals display deficits in sleep prior to accumulation of aberrant protein aggregates. Similarly, many Parkinson's patients have sleep defects prior to development of clinical characteristics typically associated with neuropathological aggregate accumulation (Gan-Or et al., 2015)(Krohn et al., 2020). Many genes that impinge on lysosomal function and sphingolipid degradation are linked to Parkinson's disease (Pan et al., 2008) (Lin et al., 2018), and glia are key regulators of Parkinson's and other neurodegenerative diseases (Zuchero and Barres, 2015)(Liddelow et al., 2017). Based on our observations, mutations in lipid-regulating genes could impair glial remodeling of specific neural circuits, including those engaged with sleep. Sleep has been proposed to drive clearance of aggregates from the brain (Xie et al., 2013)(Zhang et al., 2018), and glia are known regulators of sleep and circadian rhythms in flies and mice (Ng and Jackson, 2015) (Brancaccio et al., 2019). Our data suggest that an additional function for sleep could be to sculpt neurites via local lipid degradation, which is consistent with increased neurite volume and synapse density following sleep deprivation (Gilestro et al., 2009) (Bushey et al., 2011).

Spatiotemporal separation of lipid metabolism in the brain

Precise control of lipid species is central to many neurodegenerative models and is often modulated by neural activity (Guttenplan et al., 2021)(Liu et al., 2015)(Tsai et al., 2019)(Jung et al., 2017) (Dasgupta et al., 2009) (Acharya et al., 2003). Our data demonstrate that spatial

separation of glial Gba1b production from cyclically remodeled sLNv neurites is essential for setting the correct phase of neurite cycling, as Gba1b ectopic expression in sLNv neurons imposed an inverted cycle of membrane growth and retraction. This combined with the observations that Clock binds sphingolipid biosynthesis genes (Abruzzi et al., 2011) and that lysosome function is under circadian control (Ryzhikov et al., 2019)(Ulgherait et al., 2021) argue that lipid levels controlled by the circadian clock can orchestrate structural plasticity in the brain. Moreover, cell-type specific functions for sphingolipids are known in glia (Ghosh et al., 2013)(Kunduri et al., 2018)(Dahlgaard et al., 2012), and regional lipid heterogeneity pervades the human brain (O'Brien and Sampson, 1965). Unraveling the complicated mechanisms of cell-type specific lipid synthesis and degradation may provide crucial insights into the connections between sleep, neurodegenerative diseases, and neuronal membrane dynamics. Our data demonstrate that spatiotemporal control of sphingolipid levels via glial *gba1b* is essential to neuronal remodeling, aggregate clearance, and sleep.

Limitations of the study

Our studies revealed that the brain was highly sensitive to the level of expression of Gba1b when doing rescue experiments, likely reflecting the fact that Gba1b itself is under tight transcriptional control and that very low levels of expression are sufficient to rescue most *gba1b* phenotypes. A key gap in the fly field is the absence of tools that afford cell-type specificity, quantitative control of expression across physiologically relevant levels, and precise temporal actuation. As such tools develop, further exploring the relative balance of sphingolipid biosynthesis and degradation in shaping neurite growth and retraction would be fascinating. In addition, while analyzing sLNv neurites at specific timepoints has provided key insights, being able to capture the dynamics of lipid turnover in a live imaging preparation would deepen this understanding. This requires the application of fluorescent probes for specific lipids that can be engaged cell-type specifically, combined with a chronic imaging preparation that can span both sleep and wake cycles (as has recently been described; (Tainton-Heap et al., 2021)). Finally, while we have quantitatively measured changes in membrane lipids across the entire brain using mass spectrometry, being able to measure changes in lipid pools from specific cell types or even sub-cellular structures like neurites would likely increase the strength and specificity of these signals, thereby providing new mechanistic insights into dynamic membrane remodeling.

Acknowledgments: Research done at Stanford is conducted on Muwekma Ohlone land. We thank members of the Clandinin lab, Talbot lab, Zuchero lab, and Berfin Azizoğlu for comments on the manuscript; Estela Stevenson for technical assistance; and Tom Braukmann for assistance with the DAM computer. We are grateful to Gabor Juhaz, Joshua Mast, Ethan Perlstein, Justin Blau, Michael Rosbash, Dragana Rogulja, Marc Freeman, Thomas Montine, Gerald Rubin, and Leo Pallanck for sharing reagents. Other stocks were obtained from the Bloomington Drosophila Stock Center (NIH P40OD018537). We also gratefully acknowledge the enthusiastic support of Tom Montine and the Matloff Fund, which made this work possible. This work was supported by NIH R01EY022638 (TRC), the NSF Graduate Resource Fellowship Program (GRFP) (JV), the Stanford Developmental Biology and Genetics Graduate Training Grant (JV), and by the Stanford Vision Core grant, NIH P30EY026877 (TRC).

Author contributions:

Conceptualization: JV, ET, RJR, MTC, TRC

Methodology: JV, ET, AB, IA, IMRS, VM, MTC, TRC

Investigation: JV, ET, IMRS

Visualization: JV, ET, AB, TRC

Funding acquisition: JV, IA, TRC

Project administration: JV, VM, MTC, TRC

Supervision: VM, MTC, RJR, TRC

Writing – original draft: JV

Writing – review & editing: JV, TRC

Declaration of interests: The authors declare no competing interests

Figures and Figure Legends (combined):

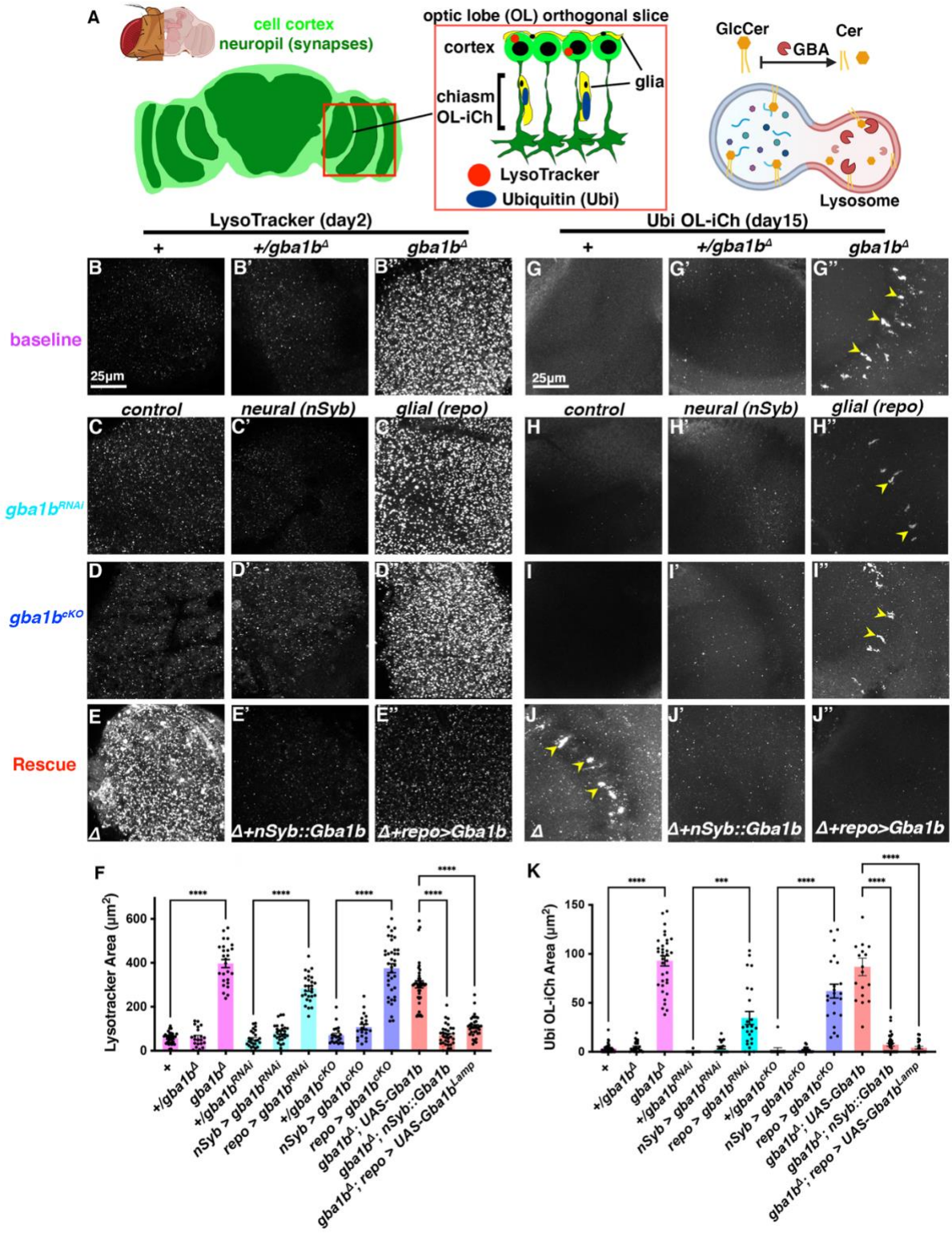
A
cell cortex
neuropil (synapses)
optic lobe (OL) orthogonal slice
cortex
glia
chiasm
OL-iCh
LysoTracker
Ubiquitin (Ubi)
GlcCer
Cer
GBA
Lysosome
LysoTracker (day2)
Ubi OL-iCh (day15)
+
+/gba1b^Δ
gba1b^Δ
baseline
gba1b^RNAi
gba1b^cKO
Rescue
control
neural (nSyb)
glial (repo)
25μm
Δ
Δ+nSyb::Gba1b
Δ+repo>Gba1b
F
Lysotracker Area (μm²)
K
Ubi OL-iCh Area (μm²)
+
+/gba1b^Δ
gba1b^Δ
+/gba1b^RNAi
nSyb > gba1b^RNAi
repo > gba1b^RNAi
+/gba1b^cKO
nSyb > gba1b^cKO
repo > gba1b^cKO
gba1b^Δ; UAS-Gba1b
gba1b^Δ; nSyb::Gba1b
gba1b^Δ; repo > UAS-Gba1b^Lamp

Figure 1. Gba1b is required in glia for lysosome function. (A) The *Drosophila* brain consists of neuronal and glial cell bodies arranged in a cortical rind (light green) enclosing dense synaptic neuropils (dark green). Within the Optic Lobe chiasm (OL-iCH), neuronal processes (dark green) are tightly associated with glial cells (yellow). Lysosomes (LysoTracker, red) are localized to cortical cell bodies (see *Figure S1*), while Ubiquitin (Ubi) aggregates are predominantly inside glia in *gba1b* mutant optic lobes (see *Figure S2*). Inside lysosomes, Gba1b degrades the lipid GlcCer into Cer. (B-E'') LysoTracker labeling in brains from 1-3 day-old flies. (G-J'') Ubiquitin aggregates in the OL-iCh in 15-20 day-old flies. (B, G) Control. (B', G') $gba1b^{\Delta 1}$/+ heterozygotes. (B'', G'') $gba1b^{\Delta 1/TT}$ transheterozygotes have enlarged lysosomes and accumulate Ubi aggregates in the OL-iCh (arrows). (C-C'', H-H'') RNA-interference, $gba1b^{RNAi}$. Control (C, H), neural (C', H'; *nSyb-GAL4*), and glial (C'', H''; *repo-GAL4*). (D-D'', I-I'') Somatic *CRISPR*, $gba1b^{cKO}$. Control (D, I), neural (D', I'; *nSyb-GAL4*), and glial (D'', I''; *repo-GAL4*). Both $gba1b^{RNAi}$ and $gba1b^{cKO}$ in glial cells but not neurons cause enlarged Lysosomes and Ubi aggregates. (E-E'', J-J'') Null $gba1b^{\Delta 1/TT}$ (E, J) can be rescued by *nSyb::Gba1b* (E', J'; neurons) or by overexpressing $UAS\text{-}Gba1b^{LAMP}$ in glia (E'', J''; *repo-GAL4*). (F) Quantification of LysoTracker data. (K) Quantification of Ubi data. *$p<0.05$, ****$p<0.0001$, ANOVA, Tukey's multiple comparisons. n>20 optic lobes. Data are represented as mean ± SEM. Scale bar: 25µm. See also *Figure S1* and *Figure S2*, and *Table S1* for genotypes.

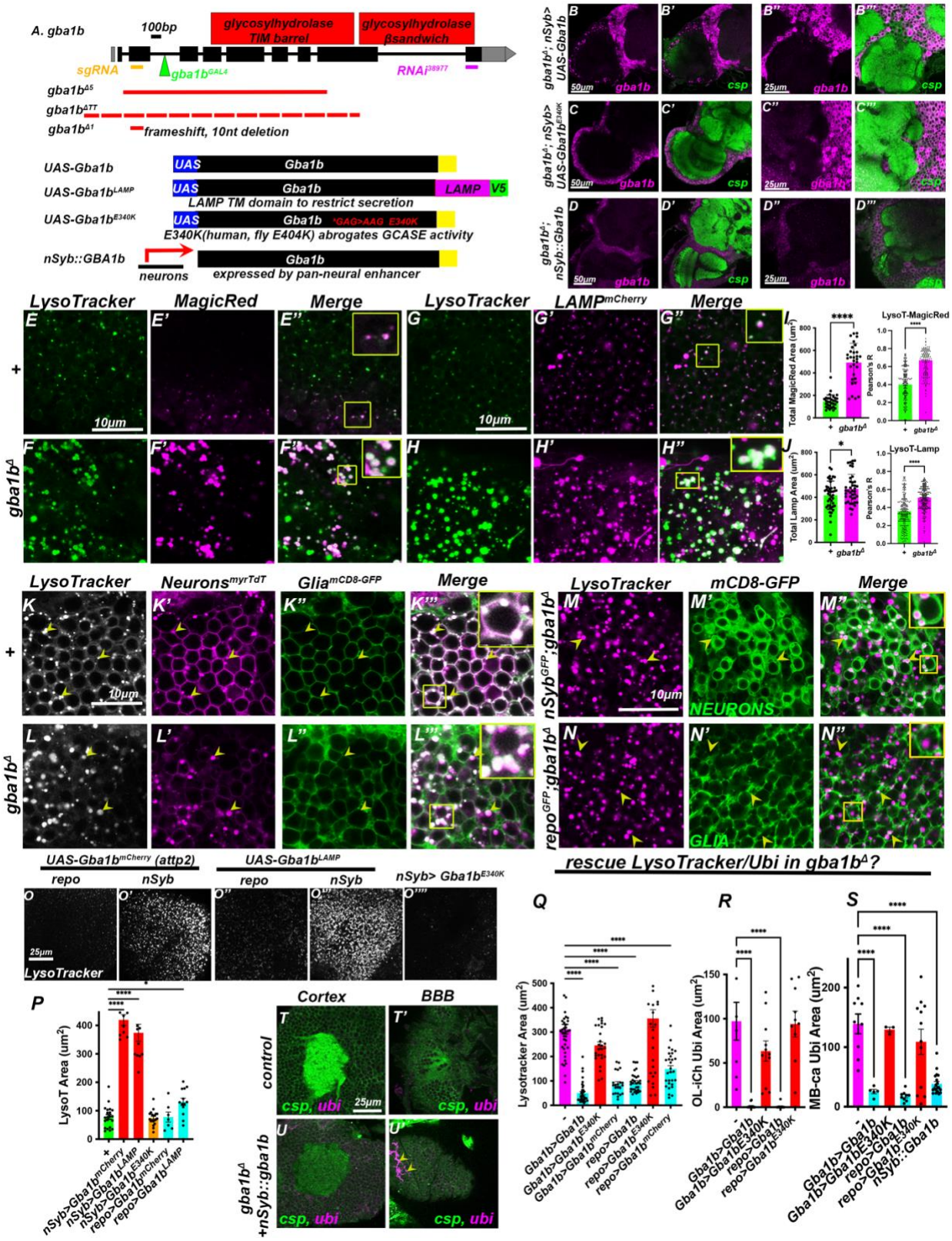
A. gba1b
100bp
glycosylhydrolase TIM barrel
glycosylhydrolase βsandwich
sgRNA
gba1b^GAL4
RNAi^38977
gba1b^Δ5
gba1b^ΔTT
gba1b^Δ1
frameshift, 10nt deletion
UAS-Gba1b
UAS-Gba1b^LAMP
LAMP TM domain to restrict secretion
UAS-Gba1b^E340K
E340K(human, fly E404K) abrogates GCASE activity
nSyb::GBA1b
neurons
expressed by pan-neural enhancer
gba1b^Δ; nSyb> UAS-Gba1b
gba1b^Δ; nSyb> UAS-Gba1b^E340K
gba1b^Δ; nSyb::Gba1b
LysoTracker
MagicRed
Merge
LAMP^mCherry
gba1b^Δ
LysoT-MagicRed
LysoT-Lamp
Neurons^myrTdT
Glia^mCD8-GFP
mCD8-GFP
nSyb^GFP;gba1b^Δ
repo^GFP;gba1b^Δ
NEURONS
GLIA
UAS-Gba1b^mCherry (attp2)
UAS-Gba1b^LAMP
nSyb> Gba1b^E340K
rescue LysoTracker/Ubi in gba1b^Δ?
Cortex
BBB
control
gba1b^Δ +nSyb::gba1b
csp, ubi

Figure S1, related to Figure 1. Gba1b genetic tools, LysoTracker labels degradative lysosomes in neurons, and rescue data. (A)The *Gba1b* locus (exons: black rectangles); target for cKO *sgRNA* (orange), $GBA^{\Delta GAL4}$ (green; also terminates transcription and is a *Gba1b* null allele (Lee et al., 2018)), and *RNAi* (purple) are indicated. *gba1b* mutants used as transheterozygous combinations are outlined by dashed red lines. $gba1b^{\Delta TT}$ deletes the 5' end of the coding sequence and *Qsox4* (not shown); $gba1b^{\Delta 5}$ flies also have a ~1.8kb insertion; $gba1b^{\Delta 1}$ generated a 10nt deletion and early frameshift. We primarily used $gba1b^{\Delta 1/TT}$ heteroallelic combinations. Also schematized are the inducible *UAS-Gba1b* minigenes used for rescue, including *mCherry* C-terminal tagged, *LAMP*-transmembrane C-terminal tagged, and an *E340K* enzyme-dead version (following the nomenclature from the *GBA1* locus in humans; fly equivalent site is E404K). Along with *UA*S-overexpression constructs we made a *Gba1b* minigene directly under the control of a neural promoter (*nSyb::Gba1b*). (B-D) Anti-Gba1b (magenta) staining of *Gba1b* transgenes with neuropil counter-stained by Csp (green). (B) *UAS-Gba1b* and (C) *UAS-*$Gba1b^{E340K}$ expressed from neural promoters (*nSyb-GAL4*) in the $gba1b^{\Delta 1/TT}$ null background strongly induced anti-Gba1b signal in neural cortex in both optic lobe and central brains. (D) In contrast, *nSyb::Gba1b* expressed at much lower levels. (E-F) Optic lobe cortex co-stained for LysoTracker and Magic Red (marking Cathepsin B activity) in control (E) and *gba1b* mutants (F), with many degradative lysosomes present in *gba1b* mutants (inset). (G-H) Optic lobe cortex co-labeled for LysoTracker and $LAMP^{mCherry}$ (lysosomal protein) in control (G) and *gba1b* mutant optic lobes (H). (I) Quantification of total area of Magic Red and colocalization analysis by Costes' method (Costes et al., 2004) and Pearson's-R. (J**)** Quantification of total area of $LAMP^{mCherry}$ and colocalization analysis by Costes' method and Pearson's-R. (K-L) Co-labeling of neural (*nSyb-GAL4*, magenta) and glial (*repo-GAL4*, white) membranes in either $gba1b^{\Delta}$ or control backgrounds identified neural membrane puncta colocalized with certain LysoTracker particles (arrows) in both mutant and control (note lack of puncta in glia). (M-N) GFP^{mCD8} expressed in neurons or glia in $gba1b^{\Delta}$ mutants revealed LysoTracker particles encircled by neural membrane but not glia membranes at the optic lobe cortex (arrows). (O-P) Gain-of-function from neural *Gba1b*-overexpression, see also *Table S1*, "GOF" sheet). LysoTracker staining of optic lobe cortex in *UAS-Gba1b* overexpressing brains (in wild-type background). Neural, but not glial, overexpression of *Gba1b* caused increased LysoTracker signal contingent on Gba1b enzyme activity as *UAS-*$Gba1b^{E340K}$ failed to cause a LysoTracker phenotype (O''''). (P) Quantification of LysoTracker data. (Q-S) summary of *UAS-Gba1b* or *UAS-*$Gba1b^{E340K}$ rescue experiments in $gba1b^{\Delta 1/TT}$ by pan-glial (*repo-GAL4*) or *Gba1b-GAL4.* Shown are LysoTracker (Q, optic lobe cortex from 2-5 day-old animals) and Ubi in Ol-iCh (R) and MB-ca (S, 15 day-old animals). Wild-type *UAS-Gba1b* but not *UAS-*$Gba1b^{E340K}$ can rescue $gba1b^{\Delta}$ phenotypes when expressed by *repo-GAL4* or $Gba1b^{GAL4}$. n>7 brains. (T-U) Ubiquitin (magenta) and neuropil (Csp, green) staining from MB-ca at both cortex and blood-brain barrier (BBB). (T-T') Control flies lack Ubi aggregates. (U-U') *nSyb::Gba1b* in $gba1b^{\Delta 1/\Delta TT}$ did rescue MB-ca aggregates (U, quantified in S) but still harbored ectopic Ubi structures in the blood-brain barrier. Scale bar: 50µm (B-B'', C-C'', D-D''), 25 µm (B''-B''', C''-C''', D''-D''', T-U), and 10µm (E-N) *p<0.05, ****p<0.0001, ANOVA, Tukey's multiple comparisons. Data are represented as mean ± SEM. See *Table S1* for genotypes and lethality/GOF summary for *UAS-Gba1b* constructs.

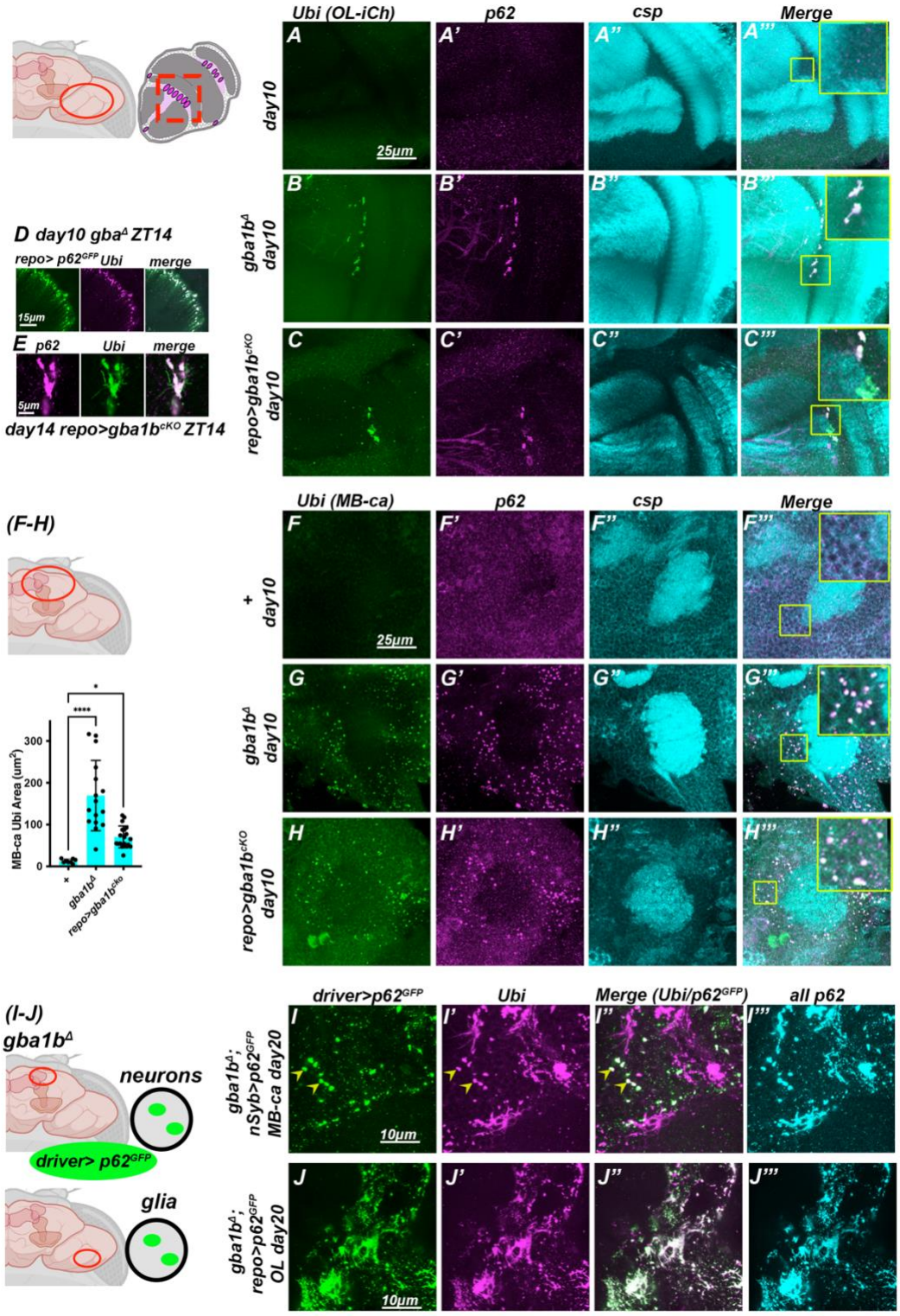
Ubi (OL-iCh)
p62
csp
Merge
A
A'
A''
A'''
day10
25µm
B
B'
B''
B'''
gba1b^Δ day10
C
C'
C''
C'''
repo>gba1b^cKO day10
D day10 gba^Δ ZT14
repo> p62^GFP Ubi
merge
15µm
E p62
Ubi
merge
5µm
day14 repo>gba1b^cKO ZT14
(F-H)
Ubi (MB-ca)
p62
csp
Merge
F
F'
F''
F'''
+ day10
25µm
G
G'
G''
G'''
gba1b^Δ day10
H
H'
H''
H'''
repo>gba1b^cKO day10
MB-ca Ubi Area (um²)
300
200
100
0
****
*
+
gba1b^Δ
repo>gba1b^cko
(I-J)
gba1b^Δ
neurons
driver> p62^GFP
glia
driver>p62^GFP
Ubi
Merge (Ubi/p62^GFP)
all p62
I
I'
I''
I'''
gba1b^Δ; nSyb>p62^GFP MB-ca day20
10µm
J
J'
J''
J'''
gba1b^Δ; repo>p62^GFP OL day20
10µm

Figure S2, related to Figure 1. Diverse, stereotyped Ubi+, p62+ aggregates pervade gba1b$^{\Delta}$ brains. (A-C’’’) OL-iCh stained for Ubi (green), p62 (magenta), and neuropil (Csp, cyan). (F-H’’’) MB-ca stained for Ubi (green), p62 (magenta), and neuropil (Csp, blue). (A-A’’’) Control brain, day 10. (B-B’’’) *gba1b$^{\Delta 1/TT}$* mutant brain, day 10. (C-C’’’) *repo>gba1b^{cKO}* mutant brain, day 10. Insets show both *gba1b* perturbations cause chiasm aggregates. (D) Co-localization of OL-iCh Ubi+ aggregates with glia-expressed *P62-GFP* (Pircs et al., 2012) in *gba1b$^{\Delta 1/TT}$*. (E) High-resolution image of a chiasm Ubi+p62+ aggregate from *repo>gba1b^{cKO}* OL-iCh. (F-F’’’) Control brain MB-Ca stained for aggregates at day 10. (G-G’’’) *gba1b$^{\Delta 1/TT}$* mutant brain MB-ca stained for aggregates at day 10. (H-H’’’) *repo>gba1b^{cKO}* mutant brain MB-ca stained for aggregates at day 10. Insets show both *gba1b* perturbations cause punctate aggregates in MB-ca cortex, quantified in leftmost graph. (I-J) *UAS-p62^{GFP}* expressed under the control of either neural or glia *GAL4* in 20-day old *gba1b$^{\Delta}$* mutant brains, stained with Ubi (magenta), GFP (green), and total p62 (cyan). (I-I’’’) Neural-expressed *p62-GFP* localized to puncta in MB-ca (arrows) but not more elaborate Ubi aggregate structures. (J-J’’’) glial-expressed *p62-GFP* colocalizes extensively with optic lobe Ubi aggregates. *p<0.05, ****p<0.0001, ANOVA, Tukey’s multiple comparisons. n>15 brains. Data are represented as mean ± SEM. Scale bar: 25µm (A-C’’’, F-H’’’), 15µm (D), 5µm (E), 15µm (I-J’’’). See *Table S1* for genotypes.

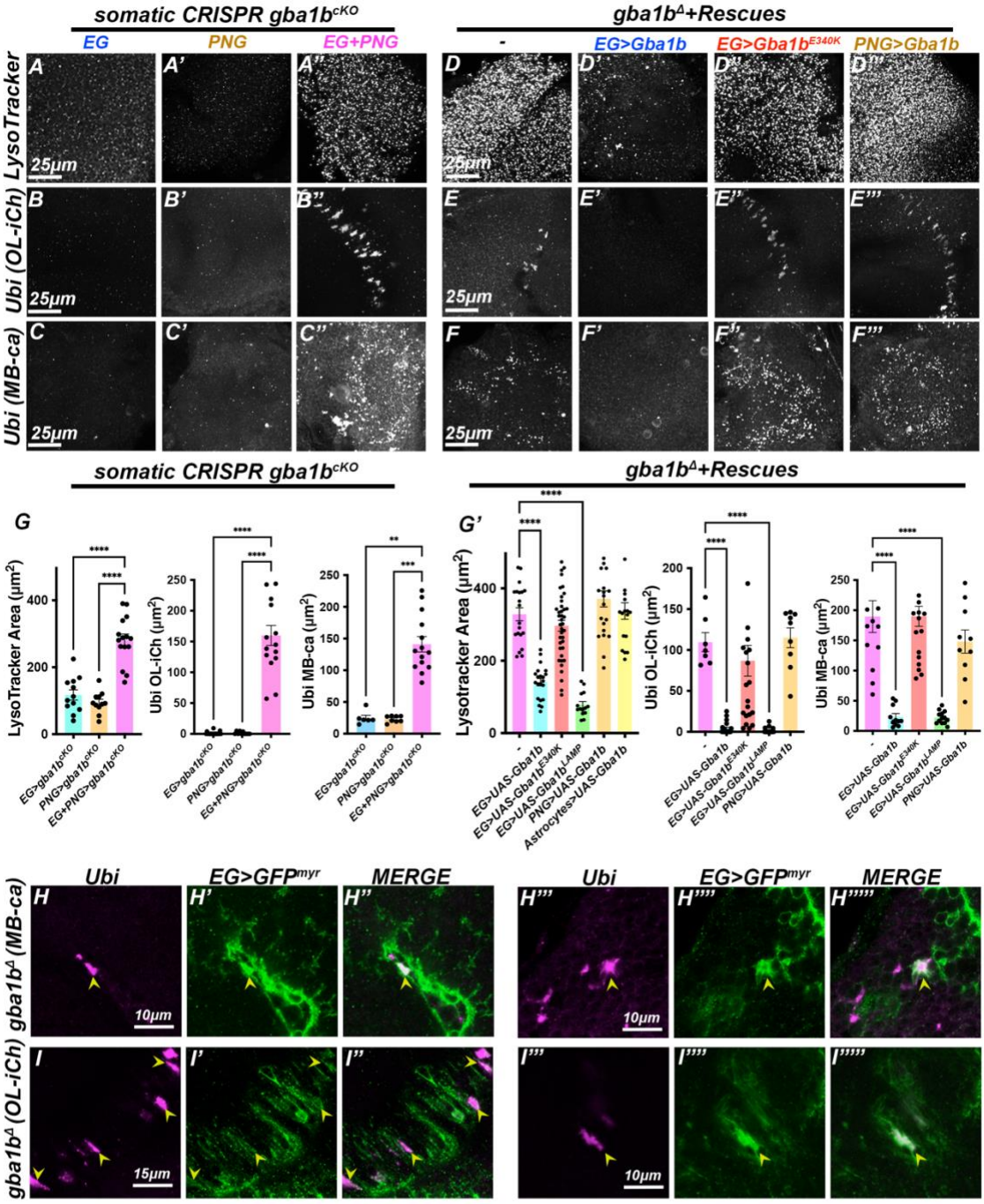
somatic CRISPR gba1b^{cKO}
EG
PNG
EG+PNG
gba1b$^{\Delta}$+Rescues
-
EG>Gba1b
EG>Gba1b^{E340K}
PNG>Gba1b
LysoTracker
Ubi (OL-iCh)
Ubi (MB-ca)
25µm
LysoTracker Area (µm^2)
Ubi OL-iCh (µm^2)
Ubi MB-ca (µm^2)
Lysotracker Area (µm^2)
EG>gba1b^{cKO}
PNG>gba1b^{cKO}
EG+PNG>gba1b^{cKO}
EG>UAS-Gba1b
EG>UAS-Gba1b^{E340K}
EG>UAS-Gba1b^{LAMP}
PNG>UAS-Gba1b
Astrocytes>UAS-Gba1b
Ubi
EG>GFP^{myr}
MERGE
gba1b$^{\Delta}$ (MB-ca)
gba1b$^{\Delta}$ (OL-iCh)
10µm
15µm

Figure 2. Specific glial subtypes are necessary and sufficient for Gba1b function in the brain. (A-C'') *gba1b* somatic *CRISPR* (*gba1b*^{cKO}) in ensheathing glia (EG, *GMR56F03*), perineural glia (PNG, *GMR85G01*), or both EG+PNG (see Figure S3 for anatomy diagram). (D-F''') Rescue of *gba1b*$^{\Delta 1/TT}$ attempted by overexpressing Gba1b in EG and PNG cell types. (A-A'', D-D''') LysoTracker labeling in 2 day-old brains. (B-B'', F-F''') Ubi labeling in 15-20 day-old brains. (A, B, C) *gba1b*^{cKO} in EG. (A', B', C') *gba1b*^{cKO} in PNG. (A'', B'', C'') *gba1b*^{cKO} in both EG and PNG caused enlarged lysosomes and Ubi aggregates. (D', E', F') Null *gba1b*$^{\Delta 1/TT}$ rescue by wild-type *UAS-Gba1b* expression in EG but not by enzyme-dead *UAS-Gba1b*^{E340K} in EG (D'', E'', F''). (D''', E''', F''') PNG expression of wild-type *UAS-Gba1b* also failed to rescue *gba1b*$^{\Delta 1/TT}$. (G) Quantification of LysoTracker data. (G') Quantification of rescue data (including data from *EG>Gba1b*^{LAMP} (green) and Astrocytes overexpressing Gba1b (yellow) for LysoTracker). (H-H''''') EG membranes (green) and subsets of Ubi (magenta) in *gba1b*$^{\Delta 1/TT}$ colocalize in the MB-ca (arrows). (I-I'') EG membranes (green) enclose Ubi (magenta) in *gba1b*$^{\Delta 1/TT}$ OL-iCh. (I'''-I''''') Subsets of OL-iCh Ubi+ structures accumulate bright EG membrane in *gba1b*$^{\Delta 1/TT}$ (arrow). *$p<0.05$, ****$p<0.0001$, ANOVA, Tukey's multiple comparisons. n>6 brains. Scale bar: 25µm (A-F); 10µm (H-H''''', I'''-I'''''), 15µm (I-I''). Data are represented as mean ± SEM. See also *Figure S3*, and *Table S1* for genotypes.

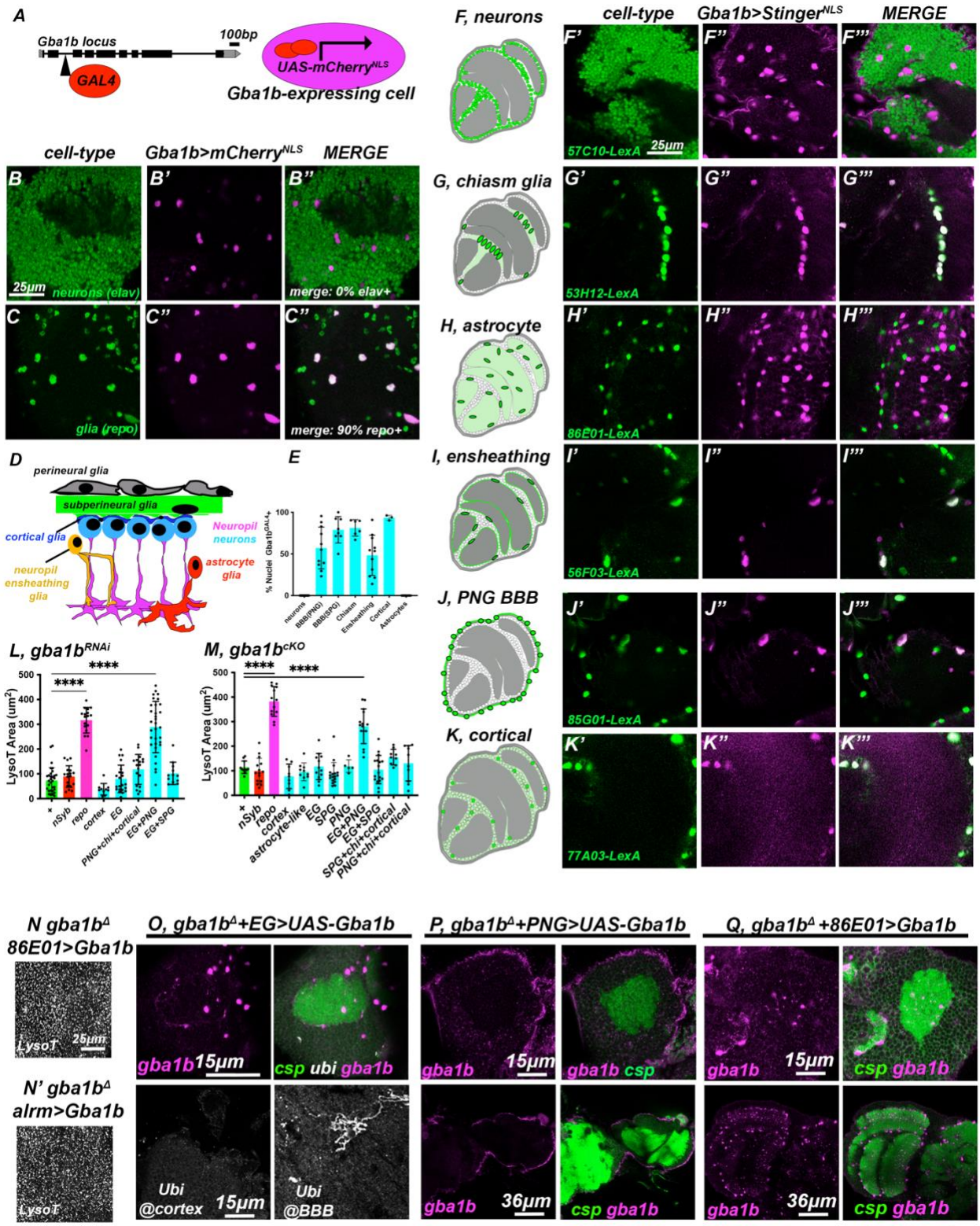
A
Gba1b locus
100bp
GAL4
UAS-mCherry^NLS
Gba1b-expressing cell
cell-type
Gba1b>mCherry^NLS
MERGE
B
B'
B''
25µm
neurons (elav)
merge: 0% elav+
C
C''
C''
glia (repo)
merge: 90% repo+
D
perineural glia
subperineural glia
cortical glia
Neuropil neurons
astrocyte glia
neuropil ensheathing glia
E
% Nuclei Gba1b^GAL4+
neurons
BBB(PNG)
BBB(SPG)
Chiasm
Ensheathing
Cortical
Astrocytes
F, neurons
cell-type
Gba1b>Stinger^NLS
MERGE
F'
F''
F'''
57C10-LexA
25µm
G, chiasm glia
G'
G''
G'''
53H12-LexA
H, astrocyte
H'
H''
H'''
86E01-LexA
I, ensheathing
I'
I''
I'''
56F03-LexA
J, PNG BBB
J'
J''
J'''
85G01-LexA
K, cortical
K'
K''
K'''
77A03-LexA
L, gba1b^RNAi
LysoT Area (um^2)
****
****
x
nSyb
repo
cortex
EG
PNG+chi+cortical
EG+PNG
EG+SPG
M, gba1b^cKO
LysoT Area (um^2)
****
****
x
nSyb
repo
cortex
astrocyte-like
EG
SPG
PNG
EG+PNG
EG+SPG
SPG+chi+cortical
PNG+chi+cortical
N gba1b^Δ
86E01>Gba1b
LysoT
25µm
N' gba1b^Δ
alrm>Gba1b
LysoT
O, gba1b^Δ+EG>UAS-Gba1b
gba1b
15µm
csp ubi gba1b
Ubi
@cortex
15µm
Ubi
@BBB
P, gba1b^Δ+PNG>UAS-Gba1b
gba1b
15µm
gba1b csp
gba1b
36µm
csp gba1b
Q, gba1b^Δ +86E01>Gba1b
gba1b
15µm
csp gba1b
gba1b
36µm
csp gba1b

Figure S3, related to Figure 2. Gba1b is expressed by glial subsets and required in both EG and PNG. (A) Schematic of the *gba1b*^{GAL4} gene trap used (Lee et al., 2018) which is expressed from the *Gba1b* locus. (B) *Gba1b*^{GAL4} drives expression of *UAS-mCherry*^{NLS} (magenta), which never colocalized with anti-elav (neurons, green) but (C) colocalized with anti-repo (glial, green). The repo-, gba1b+ cells appeared to be tracheal cells (data not shown). (D) Schematic of different glia subtypes viewed in cross section. (E) Quantification of colocalization of Gba1b+ cells with different brain cells. (F-K'') Cell-type specific orthogonal *LexA* nuclear marker (green) expression in the *Gba1b*^{GAL4} (magenta) background. Schematics show respective cell body location and neuropil tiling in green. *GMR-LexA* driver designations are included in bottom left of cell-type panels; all data are slices from optic lobes where respective cell subtypes reside. (F-F'') Neurons. (G-G'') Chiasm glia. (H-H'') Astrocyte-like glia. (I-I'') Neuropil ensheathing glia. (J-J'') Perineural glia. (K-K'') Cortical glia. (L) Quantification of LysoTracker staining of optic lobe cortex from *gba1b*^{RNAi} (BDSC#38977) driven by both single *GAL4* drivers and various combinations. Only *EG+PNG* (*GMR56F03-GAL4; GMR85G01-GAL4)* combinatorial knockdown displayed phenotypes comparable to pan-glial knockdown (*repo-GAL4*). (M) Quantification of LysoTracker from additional glia *GAL4* subtypes expressing somatic *CRISPR* (*gba1b*^{cKO}). (N) LysoTracker from *gba1b*$^{\Delta}$ optic lobes expressing Gba1b with two separate astrocyte drivers (Quantification of *GMR86E01* shown in Figure 2G'). (O) *EG-GAL4>Gba1b* expresses Gba1b (magenta) in cell bodies and around MB-ca neuropil (Csp, green) and rescues cortex Ubi (white) but fails to rescue blood-brain barrier Ubi+ present in *gba1b*$^{\Delta}$ (lower panel). (P) *PNG-GAL4>Gba1b* expresses Gba1b cell-autonomously in barrier cells in *gba1b*$^{\Delta}$, as indicated by anti-Gba1b (magenta) counterstained against neuropil (Csp, green). (Q) Astrocyte-expression of Gba1b (*GMR86E01-GAL4*) induces strong Gba1b (magenta) in astrocyte cell bodies and processes, which wrap MB-ca neuropil in upper panels (Csp, green). *$p<0.05$, ****$p<0.0001$, ANOVA, Tukey's multiple comparisons. Scale bar 25µm (A-K) and 15µm (MB-ca) or 36µm (O-Q). n>5 optic lobes. See *Table S1* for genotypes.

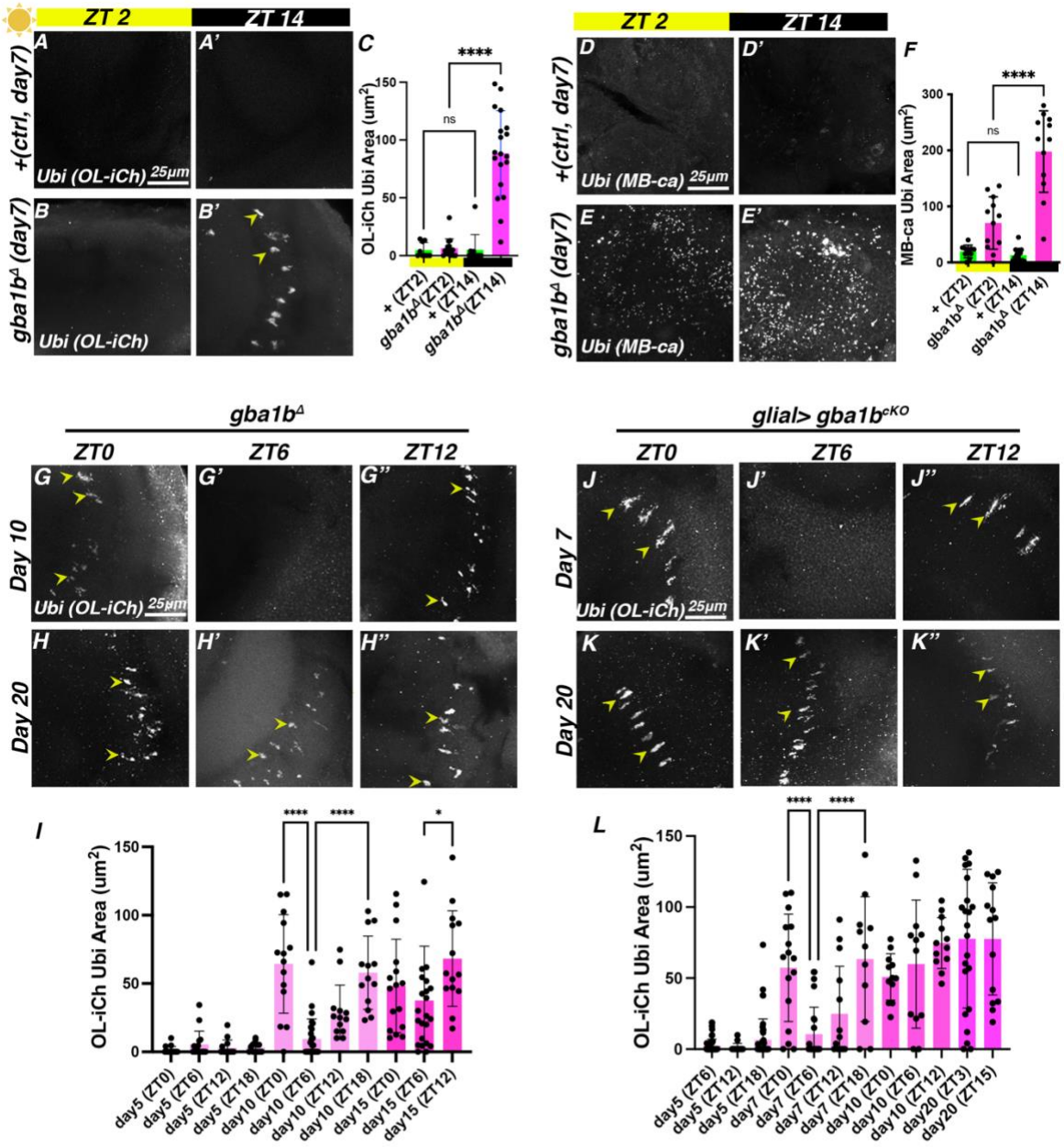
ZT 2
ZT 14
+(ctrl, day7)
gba1b^Δ (day7)
A
A'
B
B'
Ubi (OL-iCh)
25μm
C
OL-iCh Ubi Area (um²)
****
ns
+ (ZT2)
gba1b^Δ (ZT2)
+ (ZT14)
gba1b^Δ (ZT14)
D
D'
E
E'
Ubi (MB-ca)
F
MB-ca Ubi Area (um²)
gba1b^Δ
glial> gba1b^cKO
ZT0
ZT6
ZT12
Day 10
Day 20
Day 7
G
G'
G''
H
H'
H''
J
J'
J''
K
K'
K''
I
L
day5 (ZT0)
day5 (ZT6)
day5 (ZT12)
day5 (ZT18)
day10 (ZT0)
day10 (ZT6)
day10 (ZT12)
day10 (ZT18)
day15 (ZT0)
day15 (ZT6)
day15 (ZT12)
day7 (ZT0)
day7 (ZT6)
day7 (ZT12)
day7 (ZT18)
day20 (ZT0)
day20 (ZT6)
day20 (ZT12)
day20 (ZT3)
day20 (ZT15)

Figure 3. Ubiquitin aggregates cyclically grow and shrink at younger ages
Ubiquitin labeling (Ubi, white) in controls (A, A', D, D') and *gba1b*$^{\Delta 1/TT}$ transheterozygotes (B, B', E, E') examined in both the OL-iCh and the Mushroom Body calyx (MB-ca) at zeitgeber time ZT2 (day) and ZT14 (night). (I) Quantification of A-B'. (F) Quantification of D-E'. (G-H) Ol-iCh Ubi in *gba1b*$^{\Delta 1/TT}$ transheterozygotes and (I-J) glial *gba1b*^{cKO} examined at ZT0, ZT6, and ZT12 at younger (G, I) and older (H, J) ages. (K) Quantification of Ubi aggregates in *gba1b*$^{\Delta 1/TT}$ transheterozygotes across days and ZT. (L) Quantification of Ubi aggregates in glial *gba1b*^{cKO} across days and ZT. Younger *gba1b*$^{\Delta 1/TT}$ and glial *gba1b*^{cKO} brains accumulate Ubi at night and have a midday nadir (ZT6), whereas older *gba1b* flies plateau aggregates at an elevated level. *$p<0.05$, ****$p<0.0001$, ANOVA, Tukey's multiple comparisons. $n>15$ brains. Scale bar: 25µm. Data are represented as mean ± SEM. See also *Figure S4*, and *Table S1* for genotypes.

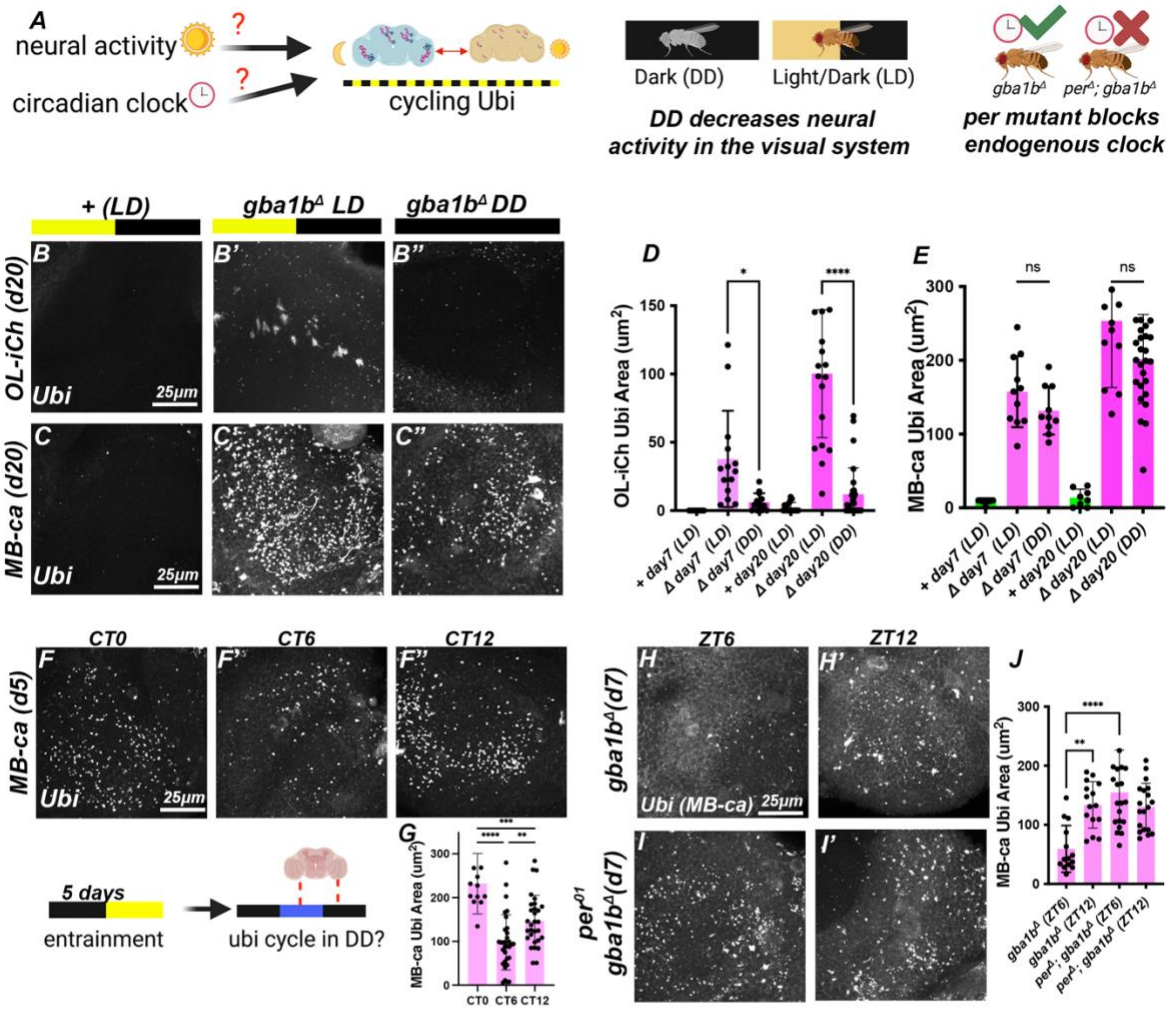
A
neural activity
circadian clock
cycling Ubi
Dark (DD)
Light/Dark (LD)
DD decreases neural activity in the visual system
gba1bΔ
perΔ; gba1bΔ
per mutant blocks endogenous clock
+ (LD)
gba1bΔ LD
gba1bΔ DD
OL-iCh (d20)
MB-ca (d20)
Ubi
25μm
OL-iCh Ubi Area (um2)
MB-ca Ubi Area (um2)
ns
CT0
CT6
CT12
MB-ca (d5)
5 days
entrainment
ubi cycle in DD?
ZT6
ZT12
gba1bΔ(d7)
perΔ1 gba1bΔ(d7)
Ubi (MB-ca)

Figure 4. Ubiquitin aggregate size is controlled by neural activity and the circadian clock. (A) Schematic of hypothesis that cycling Ubi aggregates in young *gba1b* flies are controlled by light and/or the circadian clock. (B-E) Dark-rearing reduces Ubi aggregate formation in the Ol-iCh (B) but not the MB-ca (C). (B,C) Control. (B',C') *gba1b*$^{\Delta 1/TT}$ transheterozygote raised under light-dark conditions (LD). (B'', C'') *gba1b*$^{\Delta 1/TT}$ transheterozygote raised under dark-dark conditions (DD). (D) Quantification of Ubi in the OL-iCh. (E) Quantification of Ubi in the MB-ca. Dark-rearing suppressed Ubi aggregate formation in the OL-iCh in *gba1b*$^{\Delta 1/TT}$ transheterozygotes but not the MB-ca. (F) Ubi labeling (white) in *gba1b*$^{\Delta 1/TT}$ transheterozygotes at three different circadian times (CT0, CT6, CT12) in the MB-ca after shifting entrained flies to DD conditions. (G) Quantification of MB-ca Ubi burden reveals nadir at CT6. (H-I) Ubi labeling (white) in *per*^{01}*; gba1b*$^{\Delta 1/TT}$ double mutants (I) at ZT6 and ZT12 compared to *gba1b*$^{\Delta 1/TT}$ single mutants. In younger *gba1b* brains, we observed the midday nadir of Ubi aggregate formation was lost in *per*^{01}*; gba1b*$^{\Delta 1/TT}$ double mutant animals compared to controls (quantified in J). n>15 brains. *p<0.05, ****p<0.0001, ANOVA, Tukey's multiple comparisons. Scale bar: 25µm. Data are represented as mean ± SEM. See also *Figure S4*, and *Table S1* for genotypes.

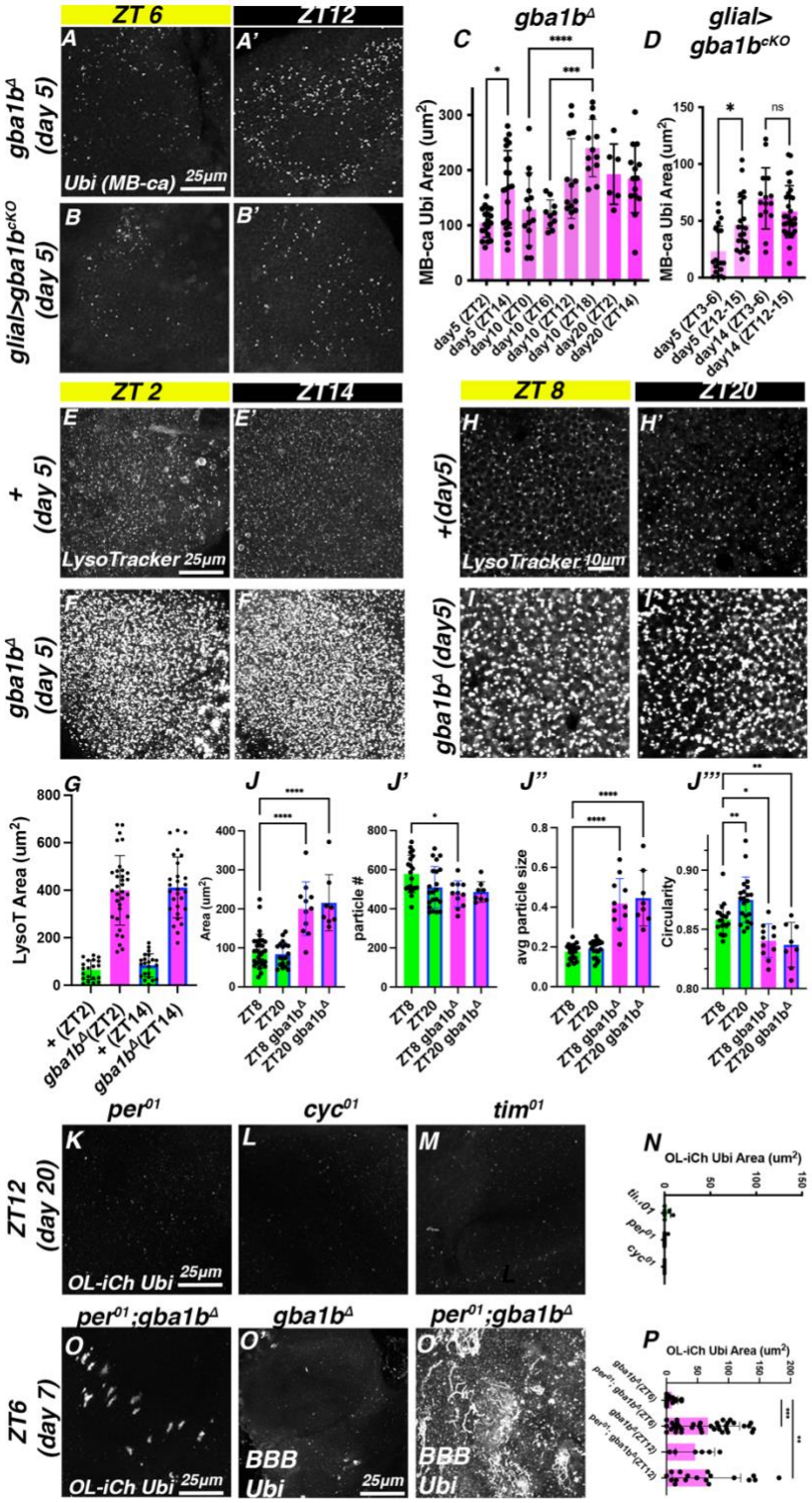
ZT 6
ZT12
gba1b^Δ (day 5)
glial>gba1b^cKO (day 5)
Ubi (MB-ca)
25μm
C
gba1b^Δ
D
glial> gba1b^cKO
MB-ca Ubi Area (um²)
day5 (ZT2)
day5 (ZT14)
day10 (ZT0)
day10 (ZT6)
day10 (ZT12)
day10 (ZT18)
day20 (ZT2)
day20 (ZT14)
day5 (ZT3-6)
day5 (Z12-15)
day14 (ZT3-6)
day14 (ZT12-15)
ns
ZT 2
ZT14
ZT 8
ZT20
+ (day 5)
+(day5)
LysoTracker
10μm
gba1b^Δ (day 5)
LysoT Area (um²)
Area (um²)
particle #
avg particle size
Circularity
+ (ZT2)
gba1b^Δ(ZT2)
+ (ZT14)
gba1b^Δ(ZT14)
ZT8
ZT20
ZT8 gba1b^Δ
ZT20 gba1b^Δ
per^01
cyc^01
tim^01
ZT12 (day 20)
OL-iCh Ubi
OL-iCh Ubi Area (um²)
per^01;gba1b^Δ
gba1b^Δ
ZT6 (day 7)
BBB Ubi

Figure S4, related to Figure 4. Additional Ubi circadian data, and circadian state has modest effects on lysosome morphology in controls. (A-A'') MB-ca Ubi structures in *gba1b*$^{\Delta 1/TT}$ or *repo>gba1b*^{cKO} mutants (B-B'') have higher aggregate burden at ZT12 than ZT6. This effect is less apparent in older animals (darker magenta, C-D). (E-F) 5 day control and *gba1b*$^{\Delta 1/TT}$ optic lobes analyzed for LysoTracker at daytime (ZT2 or ZT8) and nighttime (ZT14 or ZT20); max-intensity projections did not reveal substantial differences between the ZT conditions, with consistent elevation in *gba1b*$^{\Delta}$ over controls (G). (H-I) Higher-resolution slices of LysoTracker were used for particle analysis. (J) Particle analysis revealed subtle differences in control lysosomal populations across ZT: daytime control Lysosomes had more particles ($p = 0.056$) than nighttime and significantly more than daytime *gba1b*$^{\Delta 1/TT}$, but less circular morphology. In contrast, *gba1b*$^{\Delta 1/TT}$ brains consistently had larger but less circular LysoTracker puncta than controls at both ZT. (K-N) OL-iCh of 20 day-old circadian clock mutants at ZT12 do not have prominent Ubi structures. (O) 7 day-old, *per*^{01}*/Y; gba1b*$^{\Delta 1/TT}$ double-mutants fail to clear Ubi at ZT6 and have higher Ubi burden in the BBB than *gba1b*$^{\Delta 1/TT}$ at ZT6 (Ol-iCh quantified in P). *$p<0.05$, ****$p<0.0001$, ANOVA, Tukey's multiple comparisons. $n>15$ (A-L). $n>5$ (M-Q Scale bar: 25μm except for H (10μm). Data are represented as mean ± SEM. See *Table S1* for genotypes.

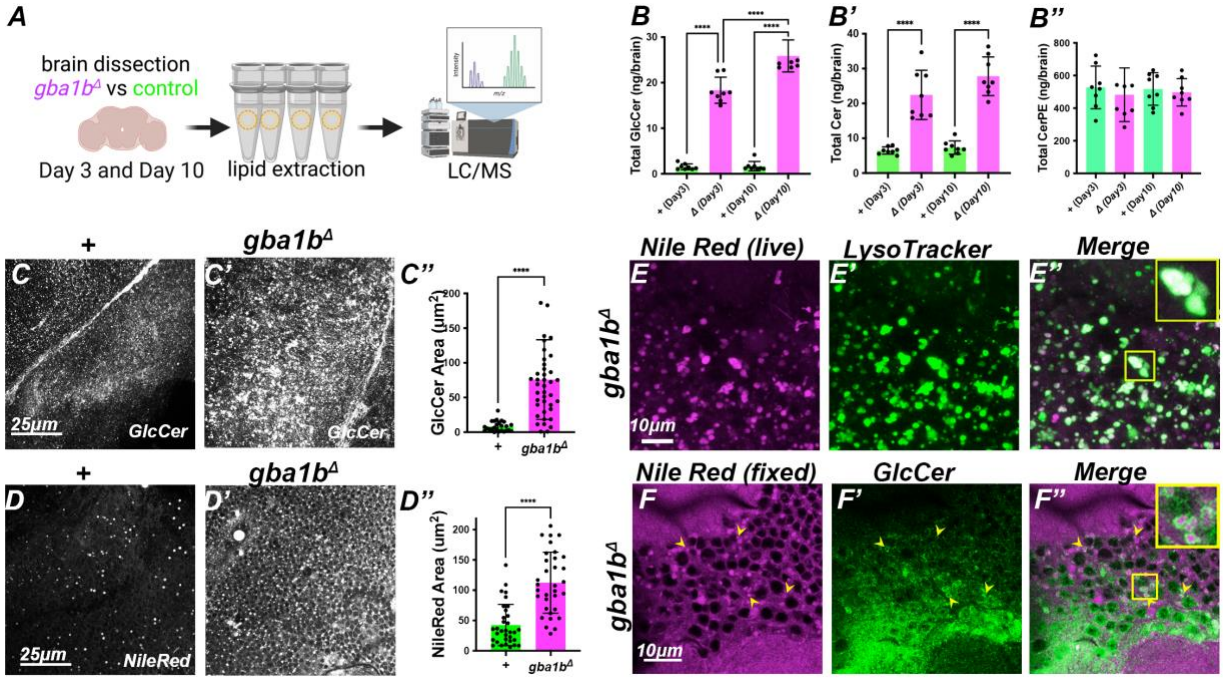

Figure 5. Specific sphingolipids accumulate in gba1b$^{\Delta}$ brains

(A) Schematic of lipidomics workflow. Brains from control and *gba1b$^{\Delta 1/TT}$* were dissected at day 3 and day 10. Lipids were extracted and then analyzed by liquid chromatography mass spectroscopy (LC-MS). (B) GlcCer levels in control (green) and *gba1b$^{\Delta 1/TT}$* mutant (magenta) brains. GlcCer abundance was elevated in mutants on day 3 with increased burden at day 10. (B') Cer levels in control (green) and *gba1b$^{\Delta 1/TT}$* mutant (magenta) brains. Cer is also elevated in *gba1b$^{\Delta 1/TT}$* mutants. (B'') CerPE levels in control (green) and *gba1b$^{\Delta 1/TT}$* mutant (magenta) brains. CerPE was unaffected; note that CerPE is present at much higher levels than Cer/GlcCer. (C) Staining against GlcCer (in OL cortex) in Control (C) and *gba1b$^{\Delta 1/TT}$* (C') at ZT12 in 5 day-old brains. (C'') Quantification of GlcCer area. *gba1b$^{\Delta 1/TT}$* mutants have increased GlcCer. (D) Staining against neutral lipids with Nile Red in Control (D) and *gba1b$^{\Delta 1/TT}$* (D') at ZT12 in 5 day-old brains. (D'') Quantification of Nile Red. *gba1b$^{\Delta 1/TT}$* mutants have increased neutral lipid burden. (E) co-labeling *gba1b$^{\Delta 1/TT}$* with Nile Red (magenta) and LysoTracker (green) in OL. LysoTracker particles are Nile Red+ (inset). (F) Fixed brains co-stained for Nile Red (magenta) and GlcCer (green) revealed that GlcCer encircled Nile Red puncta (arrowheads and inset). *p<0.05, ****p<0.0001, ANOVA, Tukey's multiple comparisons, n=15 brains/point (B) and n>10 (C-F). Data are represented as mean ± SEM. See also *Table S1* for genotypes, and *Table S3* for raw sphingolipid data.

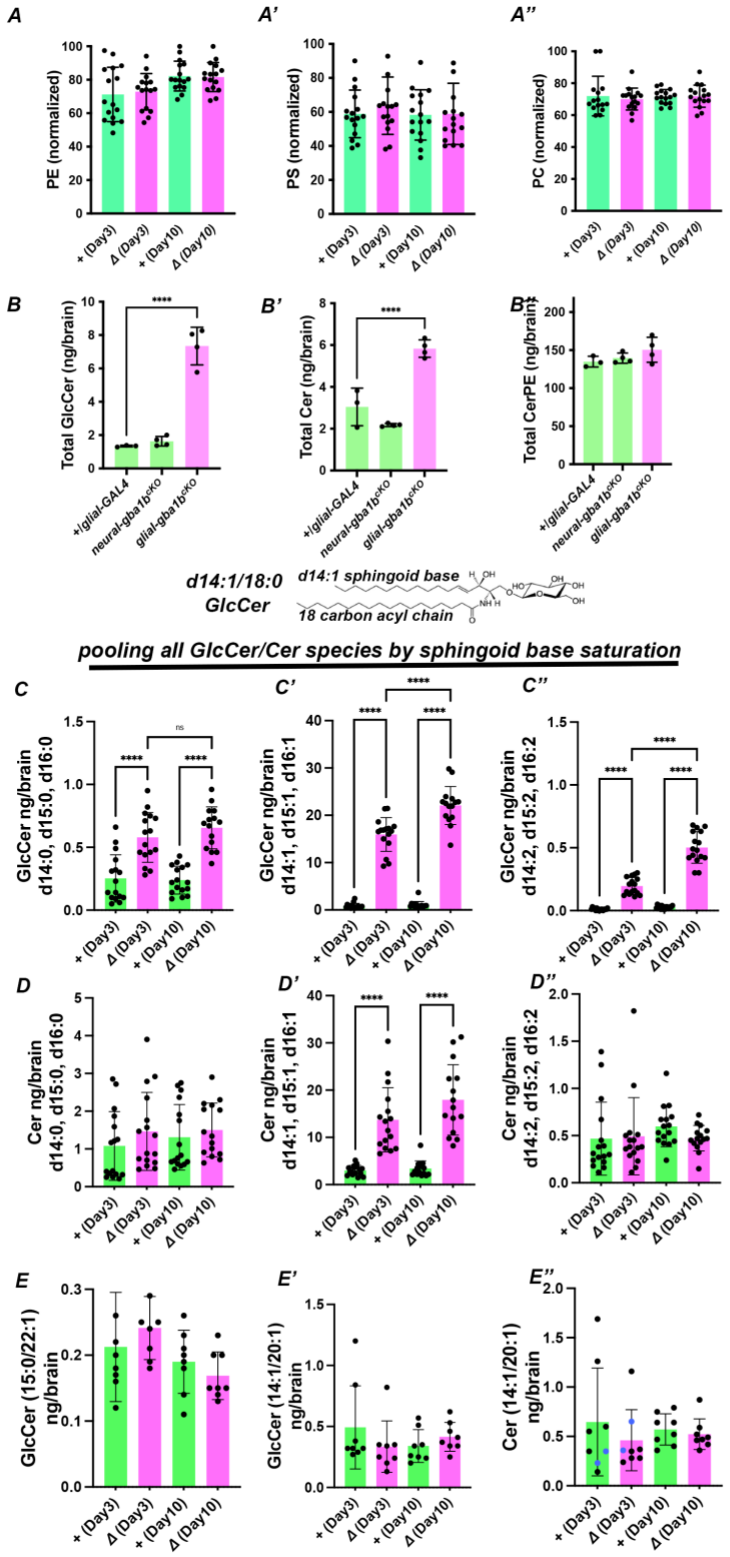
A
A'
A''
PE (normalized)
PS (normalized)
PC (normalized)
+ (Day3)
Δ (Day3)
+ (Day10)
Δ (Day10)
B
B'
B''
Total GlcCer (ng/brain)
Total Cer (ng/brain)
Total CerPE (ng/brain)
****
+/glial-GAL4
neural-gba1b^cKO
glial-gba1b^cKO
d14:1/18:0
GlcCer
d14:1 sphingoid base
18 carbon acyl chain
pooling all GlcCer/Cer species by sphingoid base saturation
C
C'
C''
GlcCer ng/brain
d14:0, d15:0, d16:0
d14:1, d15:1, d16:1
d14:2, d15:2, d16:2
ns
D
D'
D''
Cer ng/brain
E
E'
E''
GlcCer (15:0/22:1)
ng/brain
GlcCer (14:1/20:1)
Cer (14:1/20:1)

Figure S5, related to Figure 5. Further* gba1b$^{\Delta}$ *lipidomic analyses.
(A) Normalized phospholipid lipid abundance for controls (green) and *gba1b*$^{\Delta 1/TT}$ mutants (magenta) are plotted for age and zeitgeber across two independent experiments. (A) Total normalized Phosphatidylethanolamine (PE). (A') Total normalized Phosphatidylserine (PS). (A'') Total normalized Phosphatidylcholine (PC). These phospholipids were unaffected by *gba1b* removal. (B) somatic *CRISPR* removal of gba1b (*gba1b*^{cKO}) in glia (*repo-GAL4*) but not neurons (*nSyb-GAL4*) caused increased GlcCer and Cer in day 10 fly brains. (B-C) GlcCer or Cer subspecies analysis pooled by sphingoid base saturation (degree of double bonds), agnostic to fatty acyl chain length or saturation. (C, D) Saturated GlcCer and Cer species. (C',D') Monounsaturated GlcCer and Cer species. (C'', D'') diunsaturated GlcCer and Cer species. While all GlcCer species are upregulated when assayed pooled by sphingoid base, both unsaturated (dihydroceramide, D) and diunsaturated Cer species (D'') are unaffected by *gba1b*$^{\Delta}$. (E) Sphingolipids unaffected by the *gba1b* mutation included GlcCer d15:0/22:0 (E), GlcCer d14:1/20:1 (E'), and Cer d14:1/20:1 (E''); see *Table S3* for more species. *$p<0.05$, ****$p<0.0001$, ANOVA, Tukey's multiple comparisons, n=15 brains/point. Data are represented as mean ± SEM. See also *Table S1* for genotypes, and *Table S3* for raw sphingolipid data.

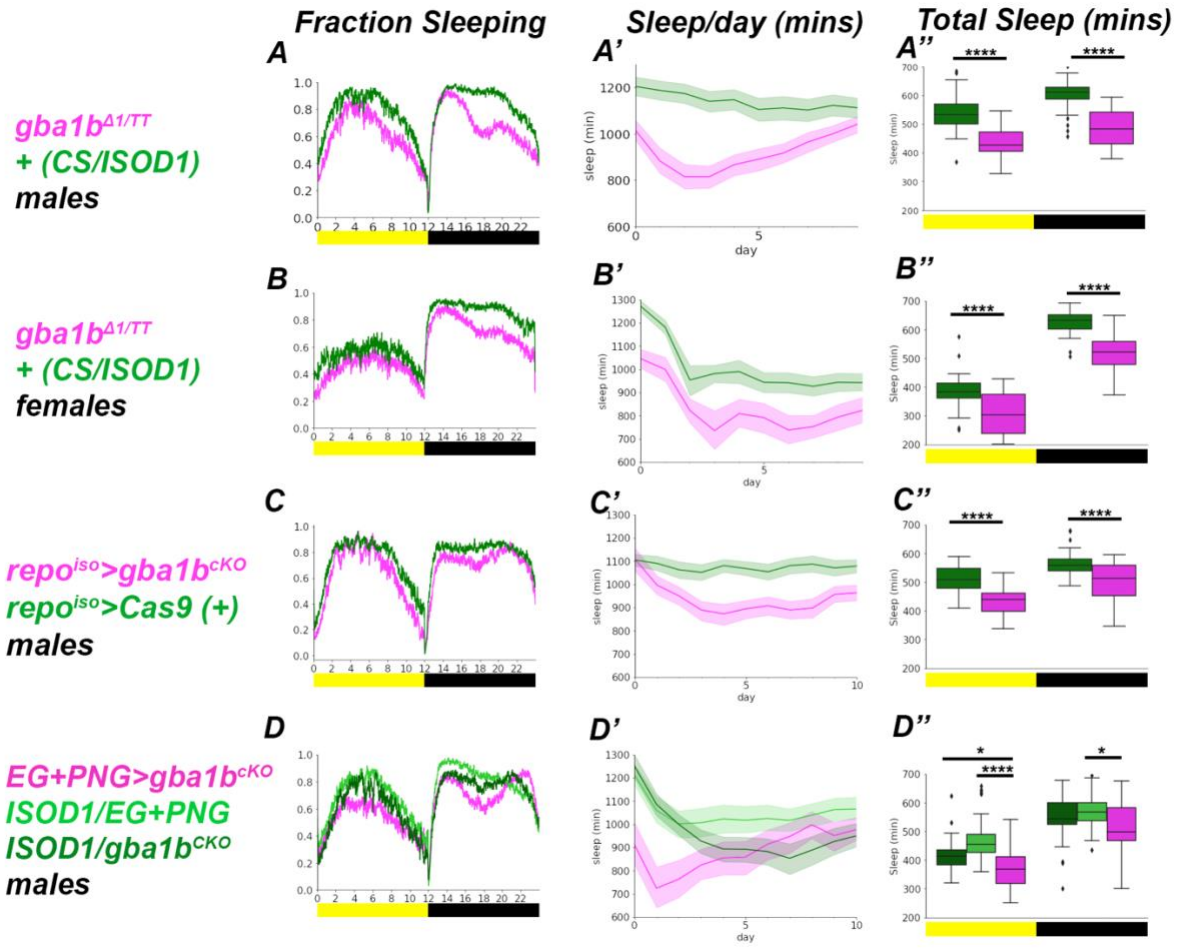

Figure 6. Sphingolipid catabolism is required for adult sleep behavior

Drosophila activity-monitor assays for measuring sleep (defined by 5 minutes of inactivity). Adult flies were analyzed post-eclosion for 10 days on a 12-hour LD cycle (yellow bars = lights-on). (A-A'') Fraction of flies asleep across ZT is reduced in male *gba1b*$^{\Delta 1/TT}$ flies (magenta) versus *CS/ISOD1* male controls (green), a defect detectable across all days (A') and for both day and night sleep (A''). (B-B'') Percent sleep across ZT is decreased in female *gba1b*$^{\Delta 1/TT}$ flies (magenta) versus *CS/ISOD1* female controls (green), a defect detectable across all days (A') and at both day and night (A''). (C-C'') Removing *gba1b* in all glia with somatic *CRISPR* (isogenized *repo-GAL4>gba1b*^{cKO}) causes a similar suite of sleep defects. (D-D'') Removing *gba1b* in EG+PNG glia (magenta, *PNG+EG>gba1b*^{cKO}) caused sleep loss compared to controls (green); we noted more variability from genetic background and stronger daytime effects. *p<0.05, ****p<0.0001, ANOVA, Tukey's multiple comparisons or Welch's ANOVA depending on equality of data variance. n>30 flies. Data are represented as mean ± SEM for Sleep/day and Total Sleep boxplots. See also *Figure S6*, and *Table S1* for genotypes.

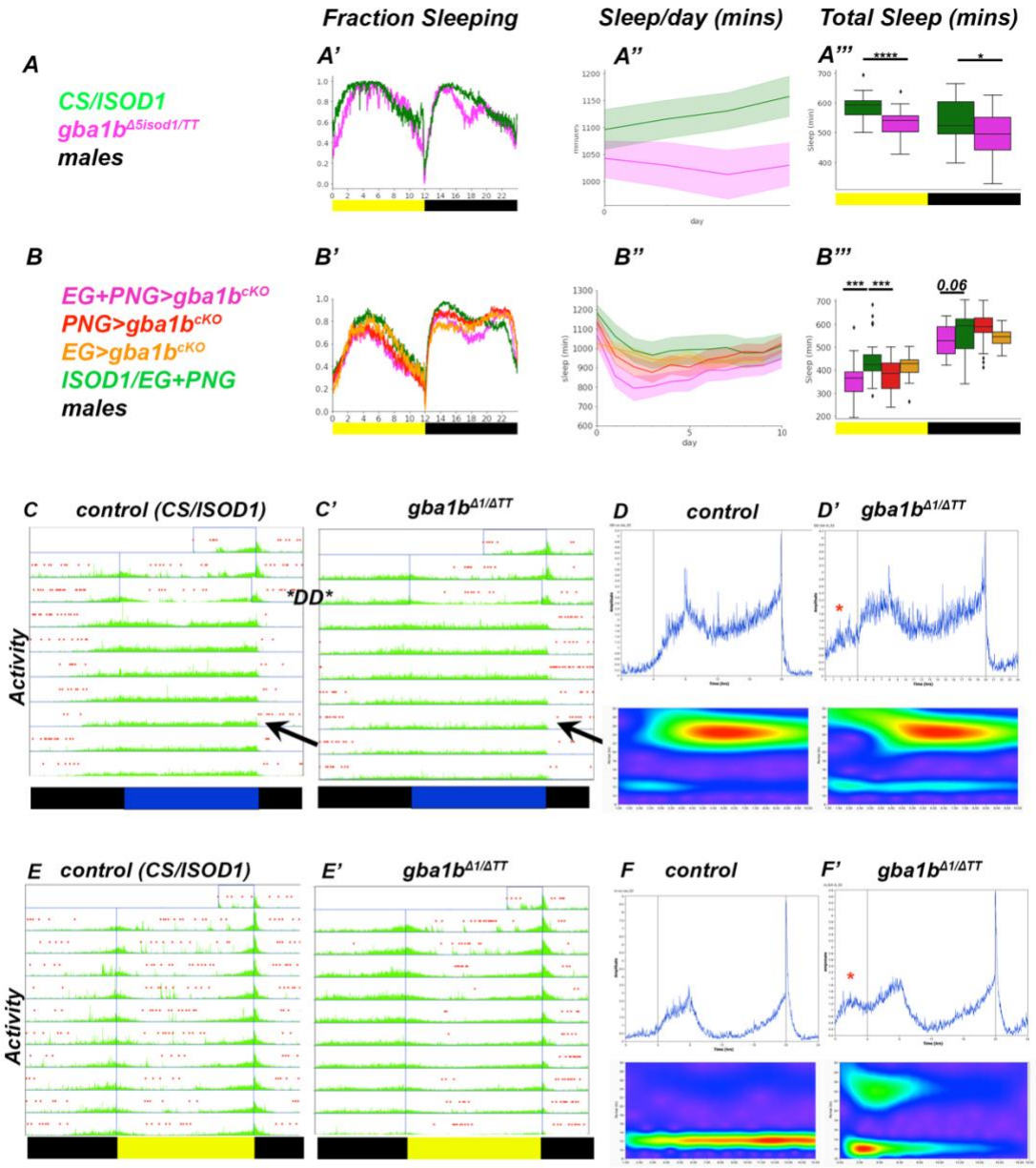
Fraction Sleeping
Sleep/day (mins)
Total Sleep (mins)
A
CS/ISOD1
gba1b$^{\Delta 5isod1/TT}$
males
A'
A''
A'''
****
*
B
EG+PNG>gba1b^{cKO}
PNG>gba1b^{cKO}
EG>gba1b^{cKO}
ISOD1/EG+PNG
males
B'
B''
B'''
***
***
0.06
C control (CS/ISOD1)
C' gba1b$^{\Delta 1/\Delta TT}$
DD
Activity
D control
D' gba1b$^{\Delta 1/\Delta TT}$
E control (CS/ISOD1)
E' gba1b$^{\Delta 1/\Delta TT}$
Activity
F control
F' gba1b$^{\Delta 1/\Delta TT}$

Figure S6, related to Figure 6. Additional DAM assays.
(A-A'') *gba1b*$^{\Delta 5/TT}$ males (magenta) also sleep less than control males (green); DAM experiment was run for 5 days from day 5 to day 10. (B-B'') Removing Gba1b in solely EG (orange) or PNG (red) using somatic *CRISPR* (*gba1b*^{cKO}) did not cause as strong a sleep defect as dual removal in both EG+PNG (magenta). (C-F') Circadian rhythm analysis in ClockLab for 5 day-old flies shifted from light-dark (LD) entrainment to dark-dark (DD) (C-D') or kept in LD (E-F'). (C) Activity traces for control flies shifted into DD (*). (C') Activity traces for *gba1b*$^{\Delta 1/TT}$ shifted to DD (*). Timely evening sleep initiation occurs at perceived lights-off (CT12, arrows). (D-D') Average activity summed over days in DD shows clear evening cessation of activity in both controls and *gba1b* mutants, and wavelet analysis in ClockLab identified periods of ~24hours for both conditions. Note increased nighttime activity in *gba1b* mutants (red *), as well as increased daytime activity in both controls and *gba1b* mutants in DD compared to LD conditions. (E-E') Average activity over LD for controls and *gba1b*$^{\Delta 1/TT}$ mutants. (F-F') Actogram and period analysis for LD control and *gba1b*$^{\Delta 1/TT}$ mutants plotted by ClockLab; *gba1b*$^{\Delta 1/TT}$ have increased nighttime activity (red *). *p<0.05, ****p<0.0001, ANOVA, Tukey's multiple comparisons or Welch's ANOVA depending on equality of data variance. n>30 flies. Data are represented as mean ± SEM for Sleep/day and Total Sleep boxplots. See *Table S1* for genotypes.

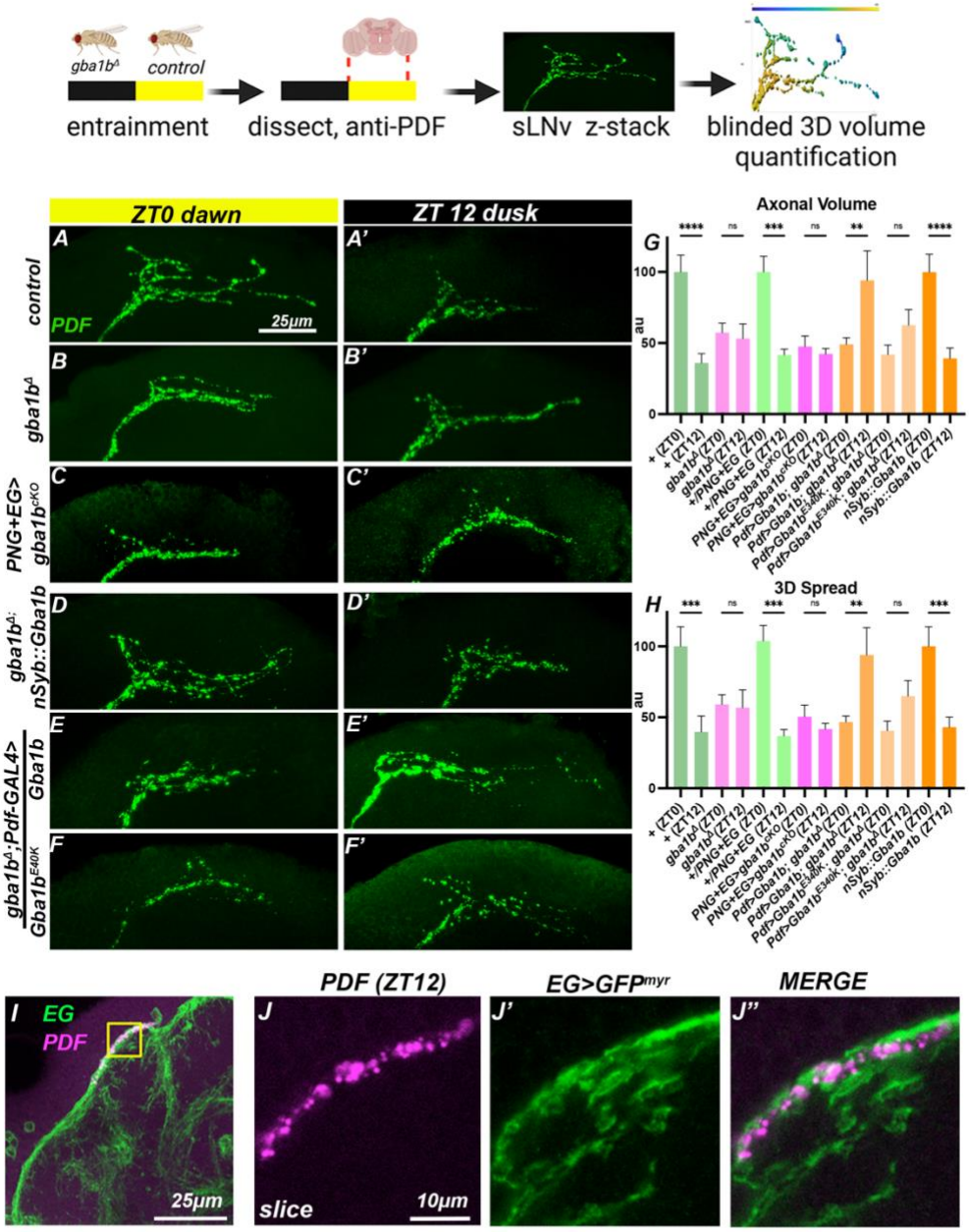
gba1b^Δ
control
entrainment
dissect, anti-PDF
sLNv z-stack
blinded 3D volume quantification
ZT0 dawn
ZT 12 dusk
control
gba1b^Δ
PNG+EG> gba1b^cKO
gba1b^Δ; nSyb::Gba1b
gba1b^Δ;Pdf-GAL4> Gba1b
Gba1b^E40K
PDF
25μm
Axonal Volume
3D Spread
au
+ (ZT0)
+ (ZT12)
gba1b^Δ (ZT0)
gba1b^Δ (ZT12)
+/PNG+EG (ZT0)
+/PNG+EG (ZT12)
PNG+EG>gba1b^cKO (ZT0)
PNG+EG>gba1b^cKO (ZT12)
Pdf>Gba1b; gba1b^Δ (ZT0)
Pdf>Gba1b; gba1b^Δ (ZT12)
Pdf>Gba1b^E40K; gba1b^Δ (ZT0)
Pdf>Gba1b^E40K; gba1b^Δ (ZT12)
nSyb::Gba1b (ZT0)
nSyb::Gba1b (ZT12)
EG
PDF
25μm
PDF (ZT12)
EG>GFP^myr
MERGE
slice
10μm

Figure 7. Sphingolipid levels drive cyclic remodeling of sLNv neurites

Schematic depicts assay for circadian sLNv neurite remodeling using anti-PDF, which faithfully represents sLNv neurite 3D morphology (Fernández et al., 2008). Following circadian entrainment, control and *gba1b*$^{\Delta 1/TT}$ brains were dissected at ZT0 (8AM, dawn) and ZT12 (8PM, dusk) and stained with anti-PDF, before acquiring 3D volumes of neurite spread. (A) Confocal projections of PDF+ sLNv neurites from 5-day old controls. Neurites are spread at dawn (ZT0) but retracted by dusk (ZT12). (B) *gba1b*$^{\Delta 1/TT}$ mutants and (C) *PNG+EG>gba1b*^{cKO} neurites fail to cycle sLNv neurites compared to controls. (D) *nSyb::Gba1b* rescued sLNv cycling in *gba1b*$^{\Delta 1/TT}$ mutants. (E) Expressing Gba1b in sLNv neurites in *gba1b*$^{\Delta 1/TT}$ using *Pdf-GAL4* inverted the remodeling cycle, with larger sLNv spread at dusk. (F) Expressing enzyme-dead *Gba1b*^{E340K} with *pdf-GAL4* in *gba1b*$^{\Delta 1/TT}$ did not cause a significant inversion of sLNv cycling. (G-H) Quantification of sLNv 3D Spread and Axonal Volume. Experiments were normalized to highest-volume control condition run in parallel with the genetic manipulations; green bars are controls, magenta bars are *gba1b* loss-of-function, and orange bars are rescue attempts in *gba1b*$^{\Delta 1/TT}$ mutants. (I-J) sLNv neurites (PDF puncta, magenta) closely juxtapose EG membranes (green) in wild-type brains. *$p<0.05$, ****$p<0.0001$, ANOVA, Tukey's multiple comparisons. n > 25 sLNv neurites (A-G), n>10 brains (I-J). Scale bar: 25µm (I), 10µm (J). Data are represented as mean ± SEM. See also *Figure S7*, and *Table S1* for genotypes.

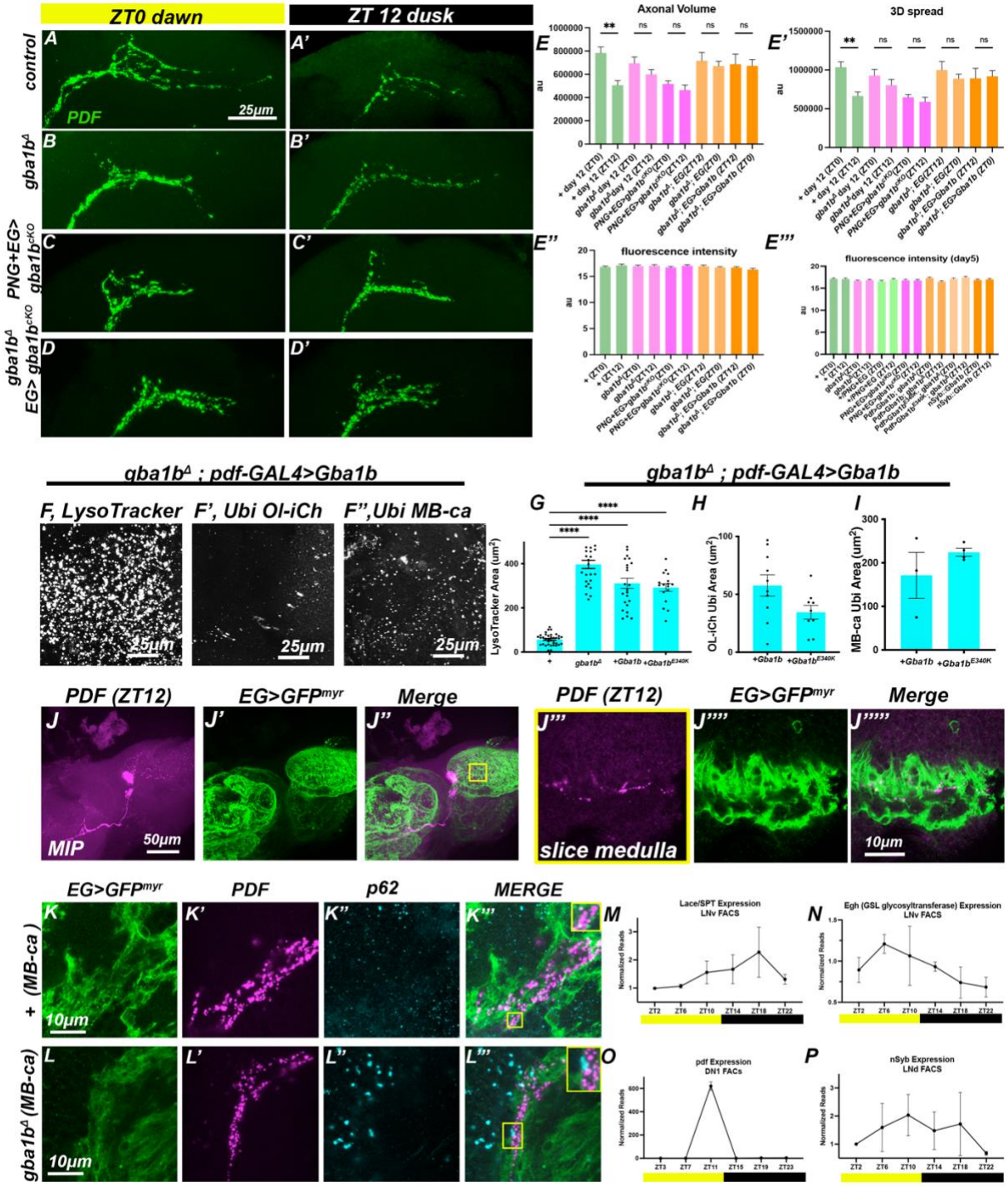
ZT0 dawn
ZT 12 dusk
control
gba1b^Δ
PNG+EG> gba1b^cKO
gba1b^Δ EG> gba1b^cKO
PDF
25µm
Axonal Volume
3D spread
fluorescence intensity
fluorescence intensity (day5)
gba1b^Δ ; pdf-GAL4>Gba1b
F, LysoTracker
F', Ubi Ol-iCh
F'',Ubi MB-ca
LysoTracker Area (um²)
OL-iCh Ubi Area (um²)
MB-ca Ubi Area (um²)
PDF (ZT12)
EG>GFP^myr
Merge
MIP
50µm
slice medulla
10µm
p62
MERGE
+ (MB-ca)
gba1b^Δ (MB-ca)
Lace/SPT Expression LNv FACS
Egh (GSL glycosyltransferase) Expression LNv FACS
pdf Expression DN1 FACs
nSyb Expression LNd FACS
Normalized Reads

Figure S7, Related to Figure 7. sLNv remodeling and* Pdf-GAL4 *rescue data.

Quantification of sLNv morphology by anti-PDF in 12 day-old flies revealed robust 3D spread and axonal volume cycling (A, quantified in E). (B) sLNv remodeling is blocked in *gba1b*$^{\Delta 1/TT}$ mutants or *PNG+EG>gba1b*^{cKO} animals (C). (D) EG overexpression of Gba1b in *gba1b*$^{\Delta 1/TT}$ failed to rescue remodeling. (E-E') Quantification of 3D spread and axonal volume. (E''-E''') Raw fluorescence intensity was unchanged between sLNv experiments. (F-I) *gba1b*$^{\Delta 1/TT}$ mutants expressing Gba1b via *Pdf-GAL4* do not rescue LysoTracker or Ubiquitin in the Ol-iCh or MB-ca, quantified in G-I. (J) sLNv neurites (PDF puncta, magenta) in wild-type optic lobes closely juxtapose EG membranes (green). (K-L) Co-labeling control (K) and *gba1b*$^{\Delta 1/TT}$ mutants (L) with anti-p62, PDF, and EG-membrane highlights proximity of MB-ca protein aggregates to EG membranes and PDF in *gba1b*$^{\Delta 1/TT}$ mutants (inset). (M-P) Data replotted from (Abruzzi et al, 2017), where various clock populations (LNv, DN1, LNd) cells were FACS-sorted and analyzed across ZT by RNA-sequencing. This dataset identified both *lace/SPT*, the rate-limiting step in sphingolipid biosynthesis, and *egghead (egh)*, a glycosyltransferase critical for making higher-order glycosphingolipids, as cycling transcripts within LNv cells. We plotted the average of this data normalized to ZT2 across two independent experiments, which revealed a strong midnight peak of *lace* expression (M). (N) *egh* expression increases following *lace* expression and is higher in the morning and midday. (O) *pdf* shows extreme peak of expression at ZT11, and PDF protein levels show corresponding increase through night to dawn(Park et al., 2000)). (P) *nSyb* was identified as weakly cycling by RNA-seq and is Clock-bound (Abruzzi et al., 2011). *p<0.05, ****p<0.0001, ANOVA, Tukey's multiple comparisons. n >24 sLNv neurites (A-D), n>15 (H), n>3 (H'-H''), n>30 (I), n>10 brains (J-L). Scale bar: 25µm (A-G), 50µm (J-J''), 10µm (J'''-J''''''', K-L). Data are represented as mean ± SEM See *Table S1* for genotypes.

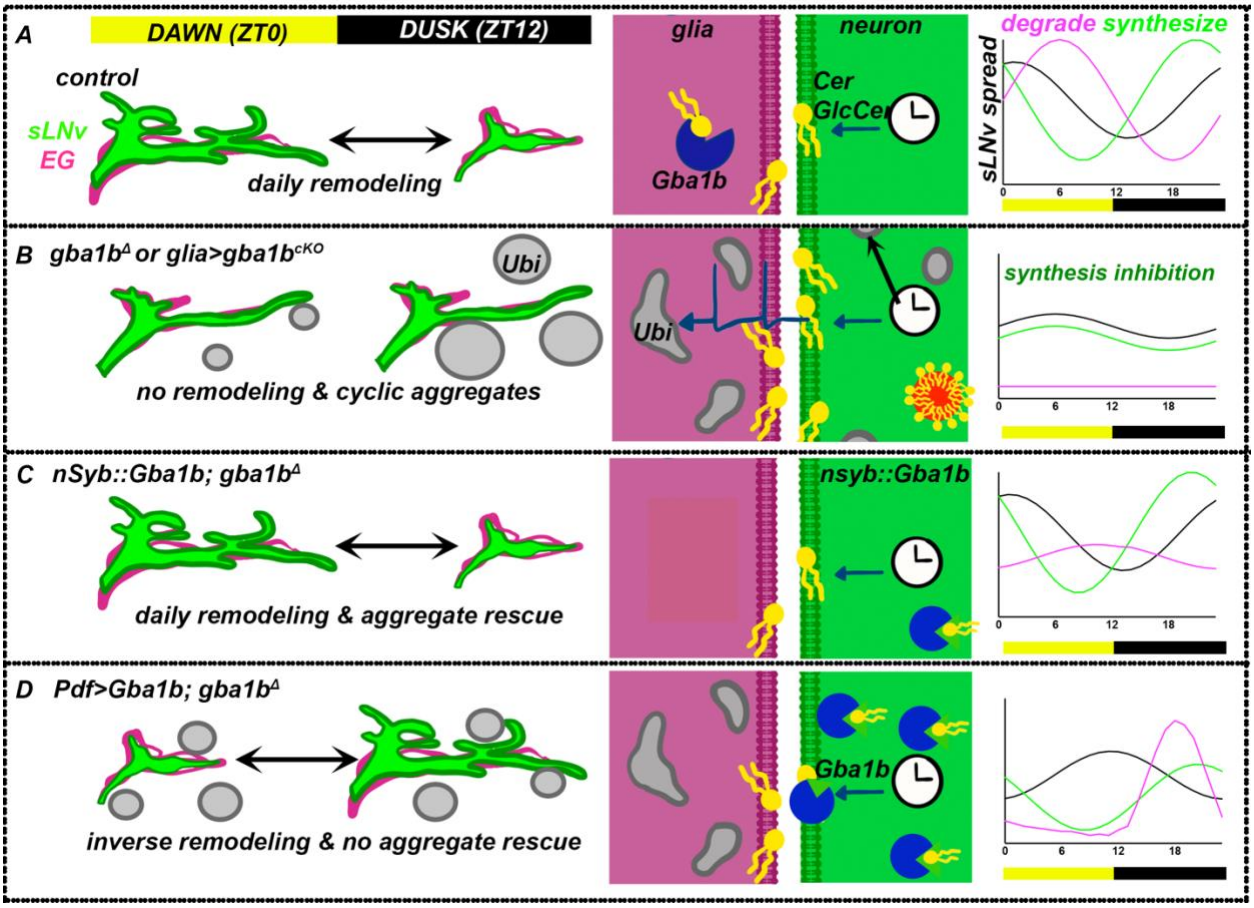

Figure 8: Glial control of sphingolipid levels sculpts diurnal remodeling of sleep circuitry. (A) In controls, sLNv neurites (green) are enclosed by ensheathing glia (EG, magenta) and remodeled daily to regulate sleep. EG produce Gba1b (blue) to locally degrade specific sphingolipids (Cer/GlcCer, yellow). Sphingolipid synthesis is controlled by the circadian clock (arrow from clock). (B) In *gba1b* perturbations, sLNv remodeling is blocked. Ubi aggregates (gray) cyclically grow at night and shrink during the day. In *gba1b* mutants, sphingolipids accumulate, including in neuronal lysosomes (red circle). Neural activity drives Ubi aggregate formation in EG in the optic lobe (blue arrow), and the clock controls mushroom body aggregates (arrow). (C) *nSyb::Gba1b* rescued sLNv cycling and aggregates in *gba1b* mutants. (D) Expressing enzyme-active Gba1b in sLNv cells in *gba1b* mutants imposes altered membrane remodeling, with greater sLNv spread at dusk, but does not rescue aggregates. (A-D, rightmost): simplified model proposing how circadian cycles of sphingolipid biosynthesis (green) and degradation (magenta) yield cyclical sLNv remodeling (black). See also *Figure S7M-P* for expression profiles of lace/SPT (*de novo* sphingolipid biosynthesis) and Pdf.

STAR Methods

KEY RESOURCES TABLE

REAGENT or RESOURCE	SOURCE	IDENTIFIER
Antibodies		
Gba1b (anti-rabbit polyclonal)	This paper, abclonal	Anti-Gba1b
Csp (anti-mouse IgG2b)	Developmental Studies Hybridoma Bank	Cat#DCSP-2 (6D6) RRID: AB_528183
Ubi (anti-mouse IgG1)	Enzo Life Sciences	Cat# BML-PW8810, RRID:AB_10541840
p62 (anti-rabbit polyclonal)	Abcam	Cat# ab178440
GFP (anti-rabbit polyclonal)	Abcam	Cat# ab13970
GlcCer (anti-rabbit polyclonal)	Glycobiotech Gmbh	Cat# RAS_0010
PDF (anti-mouse IgG2b)	Developmental Studies Hybridoma Bank	Cat# PDF C7, RRID: AB_760350)
Bruchpilot (anti-mouse IgG1)	Developmental Studies Hybridoma Bank	Cat# nc82; RRID: AB_2314866
Goat anti-Chicken IgY (H+L) Secondary Antibody, Alexa Fluor 488	moFisher Scientific	Cat# A-11039, RRID:AB_2534096)
Goat anti-Rabbit IgG (H+L) Cross-Adsorbed Secondary Antibody, Cyanine3	ThermoFisher Scientific	Cat# A10520, RRID:AB_2534029
Goat Anti-Mouse IgG2b Antibody, Alexa Fluor 488 Conjugated	ThermoFisher Scientific	Cat# A-21141, RRID:AB_141626)
Goat anti-Mouse IgG1 Cross-Adsorbed Secondary Antibody, Alexa Fluor 647	ThermoFisher Scientific	Cat# A-21240, RRID:AB_2535809)
Goat anti-Mouse IgG2b Secondary Antibody, Alexa Fluor 633	ThermoFisher Scientific	Cat# A-21146, RRID:AB_2535782)

Critical commercial assays		
LysoTracker Red DND-99	ThermoFisher Scientific	Cat# L7528
LysoTracker Deep Red	ThermoFisher Scientific	Cat# L12492
LysoTracker™ Green DND-26	ThermoFisher Scientific	Cat# L7526
MagicRed Cathepsin Assay	Abcam	Cat# ab270772
Nile Red	ThermoFisher Scientific	Cat# N1142
Experimental models: Organisms/strains		
D. melanogaster: +(ISOD1)	Clandinin lab	N/A
D. melanogaster: +(CantonS)	Clandinin lab	N/A
D. melanogaster: P{y[+t7.7] v[+t1.8]=TRiP.HMS01893}attP40	Bloomington Drosophila Stock Center	BDSC#38977, FBst0038977
D. melanogaster: gba1b[ΔTT]	Davis et al, 2016	N/A
D. melanogaster: gba1b[Δ1]	this paper	N/A
D. melanogaster: gba1b[Δ5]	Perlara (Joshua Mast)	N/A
D. melanogaster: P{y[+t7.7] v[+t1.8]=TKO.GS00895}attP40	Bloomington Drosophila Stock Center	BDSC#77100, FBst0077100
D. melanogaster: P{y[+t7.7] w[+mC]=UAS-Cas9.P2}attP2/TM6B, Tb[1]	Bloomington Drosophila Stock Center	BDSC#58986, FBst0058986
D. melanogaster: nSyb::Gba1b {attP16}	this paper	N/A
D. melanogaster: UAS-gba1b-LAMP-V5 {attP16}	this paper	N/A
D. melanogaster: UAS-gba1b-V5 {attP16}	this paper	N/A
D. melanogaster: UAS-gba1b-V5 {attP2}	this paper	N/A
D. melanogaster: UAS-gba1b[E340K]-V5 {attP2}	this paper	N/A
D. melanogaster: UAS-gba1b[E340K]-V5 {attP16}	this paper	N/A
D. melanogaster: UAS-gba1b-mCherry-V5 {attP16}	this paper	N/A
D. melanogaster: UAS-gba1b-mCherry-V5 {attP2}	this paper	N/A
D. melanogaster: TI{GFP[3xP3.cLa]=CRIMIC.TG4.0}gba1b1b[CR00541-TG4.0]/TM3, Sb[1] Ser[1]	Bloomington Drosophila Stock Center	BDSC#78943, FBst0078943
D. melanogaster: P{y[+t7.7] w[+mC]=8XLexAop2-FLPL}attP40	Bloomington Drosophila Stock Center	BDSC#55820, FBst0055820

D. melanogaster: P{13XlexAop-myr::tdTomato}attP2	Gerald Rubin	FBtp0093486
D. melanogaster: w[*]; P{w[+mC]=UAS-Stinger}2, PBac{y[+mDint2] w[+mC]=13XLexAop2-IVS-tdTomato.nls}VK00022	Bloomington Drosophila Stock Center	BDSC#66680, FBst0066680
D. melanogaster: w[*]; P{w[+mC]=UAS-mCherry.NLS}2; MKRS/TM6B, Tb[1]	Bloomington Drosophila Stock Center	BDSC#38425, FBst0038425
D. melanogaster: P{10XUAS-IVS-mCD8::GFP}attP2	Bloomington Drosophila Stock Center	BDSC#32185, FBst0032185
D. melanogaster: P{y[+t7.7] w[+mC]=GMR57C10-GAL4}attP2	Bloomington Drosophila Stock Center	BDSC#39171, FBst0039171
D. melanogaster: P{y[+t7.7] w[+mC]=GMR57C10-lexA}attP40/CyO	Bloomington Drosophila Stock Center	BDSC#52817, FBst0052817
D. melanogaster: w[1118]; P{y[+t7.7] w[+mC]=GMR77A03-GAL4}attP2	Bloomington Drosophila Stock Center	BDSC#39944, FBst0039944
D. melanogaster: w[1118]; P{y[+t7.7] w[+mC]=GMR77A03-lexA}attP40	Bloomington Drosophila Stock Center	BDSC#54108, FBst0054108
D. melanogaster: w[1118]; P{y[+t7.7] w[+mC]=GMR85G01-lexA}attP40	Bloomington Drosophila Stock Center	BDSC#54285, FBst0054285
D. melanogaster: w[1118]; P{y[+t7.7] w[+mC]=GMR85G01-GAL4}attP2	Bloomington Drosophila Stock Center	BDSC#40436, FBst0040436
D. melanogaster: w[1118]; P{y[+t7.7] w[+mC]=GMR54C07-GAL4}attP2	Bloomington Drosophila Stock Center	BDSC#50472, FBst0050472
D. melanogaster: w[1118]; P{y[+t7.7] w[+mC]=GMR54C07-lexA}attP40	Bloomington Drosophila Stock Center	BDSC#61562, FBst0061562
D. melanogaster: w[1118]; P{y[+t7.7] w[+mC]=GMR53H12-GAL4}attP2	Bloomington Drosophila Stock Center	BDSC#50456, FBst0050456
D. melanogaster: w[1118]; P{y[+t7.7] w[+mC]=GMR53H12-lexA}attP40	Bloomington Drosophila Stock Center	BDSC#53573, FBst0053573
D. melanogaster: w[1118]; P{y[+t7.7] w[+mC]=GMR56F03-GAL4}attP2	Bloomington Drosophila Stock Center	BDSC#39157, FBst0039157

D. melanogaster: w[1118]; P{y[+t7.7] w[+mC]=GMR56F03-lexA}attP40	Bloomington Drosophila Stock Center	BDSC#53574, FBst0053574
D. melanogaster: w[*]; P{y[+t7.7] w[+mC]=GMR56F03-GAL4}attP24/CyO	Bloomington Drosophila Stock Center	BDSC#77469, FBst0077469
D. melanogaster: w[*]; P{w[+mC]=nrv2-GAL4.S}3; P{nrv2-GAL4.S}8	Bloomington Drosophila Stock Center	BDSC#77469, FBst0077469
D. melanogaster: w[1118]; P{y[+t7.7] w[+mC]=GMR86E01-GAL4}attP2	Bloomington Drosophila Stock Center	BDSC#45914, FBst0045914
D. melanogaster: w[1118]; P{y[+t7.7] w[+mC]=GMR86E01-lexA}attP40/CyO	Bloomington Drosophila Stock Center	BDSC#54287, FBst0054287
D. melanogaster: w[*]; P{w[+m]=alrm-GAL4.D}3/CyO; Dr[1]/TM3, Sb[1]*	Bloomington Drosophila Stock Center	BDSC#67031, FBst0067031
D. melanogaster: w[1118]; P{y[+t7.7] w[+mC]=GMR83E12-GAL4}attP2	Bloomington Drosophila Stock Center	BDSC#40363, FBst0040363
D. melanogaster: w[1118]; P{y[+t7.7] w[+mC]=GMR83E12-lexA}attP40	Bloomington Drosophila Stock Center	BDSC#54288, FBst0054288
D. melanogaster: w[*]; P{w[+m]=moody-GAL4.SPG}2*	Bloomington Drosophila Stock Center	BDSC#90883, FBst0090883
D. melanogaster: P{w[+m]=GAL4}repo/TM3, Sb[1]*	Bloomington Drosophila Stock Center	BDSC#7415, FBst007415
D. melanogaster: per^{01}	Bloomington Drosophila Stock Center	BDSC#80928, FBst0080928
D. melanogaster: +;Pdf-GAL4;+	Dragana Rogulja	FBtp0011844
Oligonucleotides		
Primers for *Gba1b* locus sequencing, see Table S2	This paper	
Recombinant DNA		
Sequences of *Gba1b* plasmids, see Table S2	This paper	
Software and algorithms		

ImageJ (FIJI	ImageJ	RRID: SCR_003070
GraphPad Prism 9	GraphPad	RRID: SCR_002798
MATLAB_R2021a	MATLAB	RRID: SCR_001622
Python 3.7.1	Python	RRID: SCR_008394
R Studio 1.3.1093	R	RRID: SCR_000432

Table S1, detailed genotypes, n, and shorthand annotations
Table S2, sequences for primers and UAS-Gba1b plasmids
Table S3, lipidomics for sphingolipids (Cer, GlcCer, CerPE)

Materials and Methods

Lead contact

Further information and requests for resources and reagents should be directed to and will be fulfilled by the lead contact, Tom Clandinin (trc@stanford.edu).

Materials availability

Flies and plasmids are available from the lead contact, and flies will be deposited at Bloomington Drosophila Stock Center (BDSC).

Data and code availability

Sphingolipid lipidomics are deposited as Supplemental Table 3. Python code used for sleep analysis is available at https://github.com/ClandininLab/sleep_analysis. All FIJI macro scripts are available upon request. All data and information required to analyze the data in this paper are available from the lead contact upon request.

Drosophila Maintenance

Flies were maintained on standard molasses food. Freshly prepared food was used for all behavior, lipidomics, and circadian IHC/live imaging experiments. Stocks were maintained in light/dark (LD) incubators for 12:12 light:dark cycles at 24-25°C, for all experiments except those using RNAi, which were performed at 29°C. Females were used for all experiments, except as noted; however, no obvious sex differences were observed (data not shown). For circadian experiments with age-matched genotypes, virgins and males were collected and split

into independent vials housed longitudinally in the same incubator, on the same shelf (to ensure similar lighting). Individual vials were removed immediately prior to dissection.

Drosophila **Genetics**

See Table S1 for a complete list of genotypes and sample sizes. Unless otherwise stated, the control genotype was an isogenized lab-stock (*ISOD1, 75*) placed *in trans* to an independent control, *CantonS* (*CS*) ("+", *ISOD1/CS*). The *gba1b*$^{\Delta 1}$ frameshift allele (Fig. S1A) was induced by crossing *nos-Cas9* (germline *Cas9*) to a ubiquitously expressed gba1b guide (BDSC#77100) targeting an early exon to generate males carrying *nos-Cas9/gba1b*^{sgRNA} on the 2nd chromosome. These males carrying potential *gba1b*$^{\Delta ?}$ alleles were crossed to *+;+;pr/TM6b* virgins, and 10 males (*+;+;gba1b*$^{\Delta ??}$*/Tm6b*) were outcrossed to a double-balancer stock. F3 homozygotes were screened for LysoTracker phenotypes; 9/10 lines had strong *gba1b* loss-of-function LysoTracker enlargement and subsequent sequencing revealed deletions at the predicted guide locus of 1,3,6, and 10nt. The 10nt deletion, *gba1b*$^{\Delta 1}$, was used *in trans* to *gba1b*$^{\Delta TT}$ ("*gba1b*$^{\Delta}$", *gba1b*$^{\Delta 1/TT}$). In certain experiments, *gba1b*$^{\Delta 1}$ was used in *trans* to an alternative *gba1b* allele, *gba1b*$^{\Delta 5}$ (gift of Perlara and Joshua Mast), which deletes most exons (but not the start codon). *gba1b*$^{\Delta 5}$ was isogenized by backcrossing 5 generations into the *ISOD1* background and recombined with *GAL4* lines on chromosome III. *repo-GAL4* was also isogenized by backcrossing 5 generations into *ISOD1* for *repo>gba1b*^{cKO} sleep experiments. For all rescue assays with *gba1b* alleles, the presence of two *gba1b* alleles was confirmed by taking F1 siblings that failed to carry a component of the rescuing constructs (*GAL4/UAS* or otherwise) and checking for brain LysoTracker enlargement. Rescuing transgenes were checked for GAL4-independent rescue by checking *UAS-Gba1b; gba1b*$^{\Delta 1/TT}$ controls for *gba1b* loss-of-function phenotypes using LysoTracker and anti-Ubi staining.

Molecular Genetics

All *UAS-Gba1b* overexpression constructs were synthesized and cloned (Genscript) and injected into *attP* landing sites (BestGene; Table S2). *attp2* was used for all 3rd chromosome inserts, while *attP16* and *attP30* were used for 2nd chromosome, selected based on inducibilty and lower background expression than *attP40* (Markstein et al., 2008). The *pJRF7-20XUAS-IVS-mCD8::GFP* overexpression backbone harboring *attB* (Addgene # (26220, Pfeiffer et al., 2010)) was digested with XbaI and XhoI to remove intervening *mCD8-GFP*, which was replaced by a *gba1b* minigene (exons1-9 including signal sequence, omitting introns, stop codon, and UTRs); a Kozak sequence CAAA proceeds the ATG start codon before the *gba1b* minigene, and all constructs terminate with *3XSTOP* and a *SV40* terminator. In *UAS-Gba1b*^{mCherry} constructs, a NotI site and *10X-Proline* linker (GCGGCCGCGAGGTGGCGGAGGTGGCGGAGGTGGCGGAGG) were inserted prior to the *mCherry* sequence harboring an 11 N-terminal nucleotide deletion to improve *mCherry* stability and prevent cleavage from Gba1b (Huang et al, 2014). For *UAS-Gba1b*^{V5} constructs, a NotI site and 6XGly linker were inserted (GCGGCCGCGCAGCAGCAG) before a *V5* epitope tag. A cloning error caused a frameshift immediately after the NotI linker and rendered the V5 epitope unusable. For the *UAS-Gba1b*^{E340K} enzyme-dead variant, the human-equivalent of *E340K*, *E404K* in *Drosophila* (AACACGAAGTCCTGC→ AACACGGAGTCCTGC), was induced by site-directed mutagenesis and validated by sequencing (Sequetech; see Table S2 for sequencing primers). For *UAS-Gba1b*^{LAMP}, the *LAMP1* transmembrane sequence from *Drosophila* (GAAGCTCATGTAACCGCGGGAGGTGGAACGACGCCTAGCACACAGATATGATATTA

ATACCACCAAAATTAATGCAGCTAAAGCAATTCCAACGGCAATGGGAACCAC) was appended to the C-terminal of a *UAS-Gba1b-V5* backbone, following a NotI-$(GS)_5$-$(V5)_3$ linker and epitope tag. For *nSyb::Gba1b*, the 824bp promoter used in the pan-neural *nSyb* enhancer *GMR57C10* was synthesized and cloned into *UAS-Gba1b*^{E340K} by digesting with HindIII and BGIII, which deletes the *20XUAS* upstream $(5XGAL4\text{-}DBD)_4$ sequences as well as the HS promoter but leaves the *mhc IVS* intact. This places the Gba1b minigene ~100bp downstream of a strong panneural *nSyb* enhancer. Expression of constructs were validated by IHC against Gba1b, V5, or mCherry, as appropriate.

Polyclonal rabbit Gba1b antibody generation

The entire Gba1b protein minus the signal peptide (AA #22-566) was cloned into a GST-vector containing plasmid, induced and purified from inclusion bodies by Abclonal. Three New Zealand rabbits were selected based on low-background expression of pre-immunization bleeds and then immunized with Gba1b with 4 immunizations spanning 40 days. Sera was collected at 80 days and checked by Elisa for antigen reactivity. We screened test-bleeds against Gba1b-overexpressing flies and identified two bleeds which gave strong reactivity against Gba1b-specific overexpressing cells via IHC. One serum was selected for purification by antigen affinity chromatography, which labeled the Gba1b antigen at 89KD by Western Blot. While anti-Gba1b detects overexpressed Gba1b well, endogenous Gba1b expression is extremely low (Davie et al., 2018) and did not emerge above background in *gba1b*$^{\Delta 1/TT}$ or *gba1b*$^{\Delta TT/\Delta TT}$ mutant brains; it is also possible that anti-Gba1b cross-reacts with Gba1a, which is expressed at low levels in Kenyon Cells (Davie et al., 2018).

LysoTracker Brain Explant Imaging

Flies in batches of 15 were anesthetized on ice and transferred to an immobilizing plastic collar. Brains were dissected under cold 1X dissection saline (103mM NaCl, 3mM KCL, 5mM TES, 1mM NaH_2PO_4, 4mM MgCl) and placed in Terasaki plates containing 1X dissection saline before individual transfer to 12µL of freshly diluted LysoTracker solution (1:500 dilution from stock LysoTracker Red DND-99, 2µM, Thermofisher) for 2 minutes before immediate transfer to 100µL of saline on a microscope slide. Brains were pressed to the bottom of the saline bubble and oriented with dorsal side up (apposed to the coverslip). Brains were immediately imaged on a Leica SP8 confocal using a 40X Lens (N.A. 1.30) at 3X digital zoom. Z-stacks of 5 slices through the cortical region were acquired from optic lobes. Batches of 5 brains (interleaving control and experimental brains) were transferred to individual wells of Saline, LysoTracker, and individual slides in parallel. For co-staining LysoTracker with MagicRed, Nile Red, or in *Lamp*^{3XmCherry} backgrounds, LysoTracker Green DND-26 was used (also at 2µM, Thermofisher). Here, brains were incubated 2 minutes in LysoTracker green and then 2 minutes in either MagicRed (ab270772 Abcam, reconstituted in 200uL of DMSO) or Nile Red (N1142 Thermo Fisher Scientific, 1mg/mL acetone stock used 1:100 (10µg/mL final) in dissection saline) before mounting as above and immediately imaging. For imaging *myrTdT* and *GFP* flies, we used Lysotracker DeepRed, L12492 (Thermofisher) at 1:200 in dissection saline with native fluorescence for TdTomato and GFP. We were unable to reliably fix LysoTracker signals from *gba1b* brains.

IHC Dissections and Staining

As with LysoTracker, flies were anesthetized on ice and immobilized in dissection collars. The proboscis was removed under cold dissection saline and then freshly diluted 4% paraformaldehyde (PFA) was added to the dissection collar (32% EM grade PFA (EMS)). Brains were fixed for 25 minutes; after 5 minutes of immersion in 4% PFA, the remaining head cuticle and surrounding fat was gently removed. Post-fixation, brains were washed three times in 1X PBS before completing the dissection in collars and removing brains into Terasaki wells with 0.5%PBSTx (TritonX-100 0.5% in 1X PBS; for GlcCer and Nile Red staining, 0.05% PBSTx was used to better preserve lipids). Brains were permeabilized for 30 mins then transferred to blocking solution (10%NGS in 0.5%PBSTx) for 40 minutes before adding primary antibodies in 0.5%PBSTx+10%NGS (1:10 CSP, 1:200 anti-FK2 polyubiquitin, 1:500 anti-p62 (Abcam ab178440), 1:20 nc82, 1:50 anti-PDF, 1:2000 anti-Gba1b, 1:10,000 anti-GFP (Abcam ab13970), 1:500 anti-GlcCer (RAS_0010 anti-rabbit Glycobiotech) for 24-48 hours at 4°C while rocking gently. Brains were then washed three times in 1XPBS before transfer to appropriate secondaries (1:500, Thermo Fisher Scientific) and rocked at 4°C overnight. Brains were washed three times in 1XPBS before placing in 70% glycerol for clearing, then mounted and imaged in Vectashield. Images were collected using a Leica SP8 confocal microscope equipped with a 40X lens (N.A. 1.30) at 3X digital zoom. Z-stacks of 15 slices through the OL-iCh and MB-ca a were acquired to quantify Ubi aggregate formation. For circadian experiments, IHC experiments were independently repeated three times.

The following antibodies were obtained from the Developmental Studies Hybridoma Bank, created by the NICHD of the NIH and maintained at The University of Iowa, Department of Biology, Iowa City, IA 52242: CSP (6D6) developed by S. Benzer; brp (nc82) developed by E. Bruchner; and PDF (C7) developed by J. Blau.

LysoTracker/Ubiquitin particle analysis, Data Plotting

Confocal LIF files were imported into FIJI and analyzed with a custom macro. Maximum intensity projections (MIPS) of slices (equal number between control and experimental) were made and thresholded based on pixel intensity (preserving values 2 standard deviations greater than the mean). Particles were analyzed: for LysoTracker and Ubi puncta, we imposed a circularity requirement of 0.4-1 and size requirement of > 20pixels. For chiasm ubiquitin, we imposed a circularity requirement of 0.1-0.7 and size >100pixels. This FIJI macro worked well for puncta particles but occasionally missed chiasm ubiquitin or erroneously called peripheral cells as chiasm ubiquitin; thus, all analyzed MIPS and FIJI-identified particles were validated by eye post-FIJI pipeline. Particle metrics were exported to excel and graphed/analyzed by ANOVA corrected via Tukey's test for multiple comparisons in Prism GraphPad.

DAM assay and analysis

We monitored control, *gba1b*$^{\Delta}$, and *glia>gba1b*^{cKO} sleep from the first day of adult life by anesthetizing flies on ice, genotyping them, and moving into *Drosophila* Activity Monitors (DAMs, Trikinetics), where cessation of activity for 5 mins is used as a proxy for sleep. Only white+ flies were used. Males were typically unmated, and females were virgins. Data were analyzed in ClockLab as well as with a custom Python library that is available at

https://github.com/ClandininLab/sleep_analysis. Flies that were inactive for 12h prior to endpoint of the analyzed period were inferred to be dead and omitted from analysis; we noted that after ~10days of DAM housing, *gba1b*$^{\Delta}$ mutants began to move less and die, with ~50% dead by day15 (data not shown). We thus focused DAM analysis on days 1-10. Statistical analysis was done by ANOVA between control and mutant cumulative sleep binned on daytime vs nighttime; for data that was not equally variate, Welch's ANOVA was used.

sLNv assay and analysis

We entrained flies in LD (12h-light, 12h-dark), dissected control, *gba1b*$^{\Delta}$, and *PNG+EG>gba1bcKO* flies at dawn (ZT0) and dusk (ZT12), and stained brains for anti-PDF (DSHB C7 1:50) and the neuropil counterstain brp (DSHB nc82 1:20) using secondary antibodies Alexa Fluor 633 (A21126) and Alexa Fluor 488 (A21141) (following protocol in "IHC Dissections and Staining"). Both anti-PDF and *CD8-GFP* genetic labeling of sLNv cells faithfully report sLNv morphology and circadian remodeling (Fernández et al., 2008) (Petsakou et al., 2015). We acquired 1024x1024 resolution confocal stacks of ventral sLNv terminals using a Leica SP8 confocal microscope with a 40X immersion lens (N.A. 1.30) at 2X digital zoom, acquiring image planes 1µm apart. Confocal images were exported to FIJI. Analysis of 3D spread was done blind to genotype or ZT using Matlab code kindly provided by Justin Blau (Petsakou et al., 2015). We excluded brains where PdfTri neurons were not fully pruned following metamorphosis, as these PDF+ cells overlap with sLNv terminals (Helfrich-Förster, 1997). Experiments were normalized to highest-volume control condition (typically ZT0 controls) run in parallel with the genetic manipulation, as batch ICH effects changed baseline control volume parameters. All ZT0/ZT12 experiments were dissected on the same day.

Lipidomics and analysis

Fly cohorts of control (*CS/ISOD1)* and *gba1b*$^{\Delta 1/TT}$ mutants were housed in antiphase incubators and dissected at ZT16-18 (night/asleep) or ZT10-12 (day/awake, evening peak of activity) at day 3 and day 10. For Figure 5 and Figure S5, day 3 and day 10 brains were pooled across the two dissection ZTs. Crosses were maintained in 12:12 light/dark (LD) incubators that were at 25°C and 50-70% humidity. Light lux was estimated to be ~400 lumens. For dissections during 'night', flies were removed from incubators in aluminum-foil enclosed boxes and not exposed to light until dissection.

15 brains per condition (genotype/timepoint) were dissected in quadruplicate (4 separate tubes). Dissections were in 1X dissection saline (see "IHC dissections" above). Flies were anesthetized on ice; all non-brain tissue (fat/hemocytes, larger trachea) was removed, as well as retina (entirely) and most lamina. Single dissected brains were immediately transferred to Eppendorf tubes containing 20µl saline on ice; after 15 brains were added (10-15mins), 180µl of methanol was added (90% methanol v/v) and brains were snap-frozen on dry ice and stored at -80°C until further analysis. The main lipidomics experiment conducted across day3/day10 was repeated in duplicate twice with independent genetic crosses.

From each group of 15 brains, 10brains were analyzed for sphingolipids and phospholipids. Brain total lipids containing internal standards (ISTD) were extracted as described by *(61)*. ISTD used

included GlucosylßCeramide d18:1/8:0 (Avanti #860540), CerPE d18:1/24:0 (Avanti #860067) and Equisplash™ LIPIDOMIX® Quantitative Mass Spec Internal Standard (Avanti #330731). Lipid extracts were separate by normal phase chromatography (Agilent Zorbax RX-Sil column 3.0 x 100 mm, 1.8 µm particle size) using an Agilent 1260 Infinity LC system (Santa Clara, CA). The total LC run time was 38 min (with 5 min post-run) at a flow rate of 0.3 µL/min. Mobile phase A was composed of isopropanol/hexane/water (58:40:2,v/v) with 5mM ammonium acetate and 0.1% acetic acid. Mobile phase B consisted of isopropanol/hexane/water (50:40:10,v/v) with 5mM ammonium acetate and 0.1% acetic acid. Gradient elution consisted of increase from 34 to 36 min until 100% of mobile phase B, and after 36 min the mobile phase decreased to 0% for 2 more min. All MS measurements were obtained using an Agilent 6430 Triple-Quad LC/MS system (Santa Clara, CA) operating in positive ion mode. Gas-phase ions of various lipid species were obtained using electrospray ionization (ESI). The MS was operated in multiple reaction monitoring (MRM). The collision energies vary from 15 to 45 eV. Data acquisition and analysis was carried out using the Agilent Mass Hunter software package.

For Cer, GlcCer, and CerPE, total ng/lipid species were calculated per brain per tube. We report raw values in *Table 3* but for certain figures report values normalized to the highest ng/brain value per experiment run for that sphingolipid class (for cases where substantial batch variation occurred between 2 experiments). For subspecies analysis, we normalized values to highest ng/brain value for individual lipid species across the experimental run; total lipids detected (ng/brain) was unchanged between mutants and controls in both experiments. For phospholipids, total ng/lipid species were calculable for PE/PS/PC; both raw and normalized values for PE, PS, and PC showed no significant difference between mutant and control at matched ZT or age.

References

Abruzzi, K.C., Rodriguez, J., Menet, J.S., Desrochers, J., Zadina, A., Luo, W., Tkachev, S., and Rosbash, M. (2011). *Drosophila* CLOCK target gene characterization: implications for circadian tissue-specific gene expression. Genes Dev. *25*, 2374–2386.

Abruzzi, K.C., Zadina, A., Luo, W., Wiyanto, E., Rahman, R., Guo, F., Shafer, O., and Rosbash, M. (2017). RNA-seq analysis of Drosophila clock and non-clock neurons reveals neuron-specific cycling and novel candidate neuropeptides. PLOS Genetics *13*, e1006613.

Acharya, U., and Acharya, J.K. (2005). Enzymes of sphingolipid metabolism in Drosophila melanogaster. Cell Mol Life Sci *62*, 128–142.

Acharya, U., Patel, S., Koundakjian, E., Nagashima, K., Han, X., and Acharya, J.K. (2003). Modulating sphingolipid biosynthetic pathway rescues photoreceptor degeneration. Science *299*, 1740–1743.

Artiushin, G., Zhang, S.L., Tricoire, H., and Sehgal, A. (2018). Endocytosis at the Drosophila blood–brain barrier as a function for sleep. ELife *7*, e43326.

Awad, O., Sarkar, C., Panicker, L.M., Miller, D., Zeng, X., Sgambato, J.A., Lipinski, M.M., and Feldman, R.A. (2015). Altered TFEB-mediated lysosomal biogenesis in Gaucher disease iPSC-derived neuronal cells. Hum Mol Genet *24*, 5775–5788.

Barth, M., Hirsch, H.V.B., Meinertzhagen, I.A., and Heisenberg, M. (1997). Experience-Dependent Developmental Plasticity in the Optic Lobe of Drosophila melanogaster. J. Neurosci. *17*, 1493–1504.

Bartlett, B.J., Isakson, P., Lewerenz, J., Sanchez, H., Kotzebue, R.W., Cumming, R.C., Harris, G.L., Nezis, I.P., Schubert, D.R., Simonsen, A., et al. (2011). p62, Ref(2)P and ubiquitinated proteins are conserved markers of neuronal aging, aggregate formation and progressive autophagic defects. Autophagy *7*, 572–583.

Becquet, D., Girardet, C., Guillaumond, F., François-Bellan, A.-M., and Bosler, O. (2008). Ultrastructural plasticity in the rat suprachiasmatic nucleus. Possible involvement in clock entrainment. Glia *56*, 294–305.

Bedont, J.L., Toda, H., Shi, M., Park, C.H., Quake, C., Stein, C., Kolesnik, A., and Sehgal, A. (2021). Short and long sleeping mutants reveal links between sleep and macroautophagy. Elife *10*, e64140.

Brancaccio, M., Edwards, M.D., Patton, A.P., Smyllie, N.J., Chesham, J.E., Maywood, E.S., and Hastings, M.H. (2019). Cell-autonomous clock of astrocytes drives circadian behavior in mammals. Science *363*, 187–192.

Bushey, D., Tononi, G., and Cirelli, C. (2011). Sleep and synaptic homeostasis: structural evidence in Drosophila. Science *332*, 1576–1581.

Cangalaya, C., Stoyanov, S., Fischer, K.-D., and Dityatev, A. (2020). Light-induced engagement of microglia to focally remodel synapses in the adult brain. ELife *9*, e58435.

Choi, C., Cao, G., Tanenhaus, A.K., McCarthy, E. v., Jung, M., Schleyer, W., Shang, Y., Rosbash, M., Yin, J.C.P., and Nitabach, M.N. (2012). Autoreceptor Control of Peptide/Neurotransmitter Corelease from PDF Neurons Determines Allocation of Circadian Activity in Drosophila. Cell Reports *2*, 332–344.

Clark, G.T., Yu, Y., Urban, C.A., Fu, G., Wang, C., Zhang, F., Linhardt, R.J., and Hurley, J.M. (2022). Circadian control of heparan sulfate levels times phagocytosis of amyloid beta aggregates. PLOS Genetics *18*, e1009994.

Dahlgaard, K., Jung, A., Qvortrup, K., Clausen, H., Kjaerulff, O., and Wandall, H.H. (2012). Neurofibromatosis-like phenotype in Drosophila caused by lack of glucosylceramide extension. Proc Natl Acad Sci U S A *109*, 6987–6992.

Dasgupta, U., Bamba, T., Chiantia, S., Karim, P., Tayoun, A.N.A., Yonamine, I., Rawat, S.S., Rao, R.P., Nagashima, K., Fukusaki, E., et al. (2009). Ceramide kinase regulates phospholipase C and phosphatidylinositol 4, 5, bisphosphate in phototransduction. PNAS *106*, 20063–20068.

Davie, K., Janssens, J., Koldere, D., Waegeneer, M.D., Pech, U., Kreft, Ł., Aibar, S., Makhzami, S., Christiaens, V., González-Blas, C.B., et al. (2018). A Single-Cell Transcriptome Atlas of the Aging Drosophila Brain. Cell *174*, 982-998.e20.

Davis, M.Y., Trinh, K., Thomas, R.E., Yu, S., Germanos, A.A., Whitley, B.N., Sardi, S.P., Montine, T.J., and Pallanck, L.J. (2016). Glucocerebrosidase Deficiency in Drosophila Results in α-Synuclein-Independent Protein Aggregation and Neurodegeneration. PLOS Genetics *12*, e1005944.

Doherty, J., Logan, M.A., Tasdemir, O.E., and Freeman, M.R. (2009). Ensheathing Glia Function as Phagocytes in the Adult Drosophila Brain. Journal of Neuroscience *29*, 4768–4781.

Enquist, I.B., Lo Bianco, C., Ooka, A., Nilsson, E., Månsson, J.-E., Ehinger, M., Richter, J., Brady, R.O., Kirik, D., and Karlsson, S. (2007). Murine models of acute neuronopathic Gaucher disease. Proc Natl Acad Sci U S A *104*, 17483–17488.

Fernández, M.P., Berni, J., and Ceriani, M.F. (2008). Circadian remodeling of neuronal circuits involved in rhythmic behavior. PLoS Biol *6*, e69.

Fitzner, D., Bader, J.M., Penkert, H., Bergner, C.G., Su, M., Weil, M.-T., Surma, M.A., Mann, M., Klose, C., and Simons, M. (2020). Cell-Type- and Brain-Region-Resolved Mouse Brain Lipidome. Cell Reports *32*, 108132.

Freeman, M.R. (2015). Drosophila Central Nervous System Glia. Cold Spring Harb Perspect Biol *7*, a020552.

Futerman, A.H., and van Meer, G. (2004). The cell biology of lysosomal storage disorders. Nat Rev Mol Cell Biol *5*, 554–565.

Gan-Or, Z., Mirelman, A., Postuma, R.B., Arnulf, I., Bar-Shira, A., Dauvilliers, Y., Desautels, A., Gagnon, J.-F., Leblond, C.S., Frauscher, B., et al. (2015). GBA mutations are associated with Rapid Eye Movement Sleep Behavior Disorder. Ann Clin Transl Neurol *2*, 941–945.

Ghosh, A., Kling, T., Snaidero, N., Sampaio, J.L., Shevchenko, A., Gras, H., Geurten, B., Göpfert, M.C., Schulz, J.B., Voigt, A., et al. (2013). A Global In Vivo Drosophila RNAi Screen Identifies a Key Role of Ceramide Phosphoethanolamine for Glial Ensheathment of Axons. PLOS Genetics *9*, e1003980.

Gilestro, G.F., Tononi, G., and Cirelli, C. (2009). Widespread Changes in Synaptic Markers as a Function of Sleep and Wakefulness in Drosophila. Science *324*, 109–112.

Grima, B., Chélot, E., Xia, R., and Rouyer, F. (2004). Morning and evening peaks of activity rely on different clock neurons of the Drosophila brain. Nature *431*, 869–873.

Guttenplan, K.A., Weigel, M.K., Prakash, P., Wijewardhane, P.R., Hasel, P., Rufen-Blanchette, U., Münch, A.E., Blum, J.A., Fine, J., Neal, M.C., et al. (2021). Neurotoxic reactive astrocytes induce cell death via saturated lipids. Nature *599*, 102–107.

Heisenberg, M., Heusipp, M., and Wanke, C. (1995). Structural plasticity in the Drosophila brain. J. Neurosci. *15*, 1951–1960.

Helfrich-Förster, C. (1997). Development of pigment-dispersing hormone-immunoreactive neurons in the nervous system of Drosophila melanogaster. Journal of Comparative Neurology *380*, 335–354.

Helfrich-Förster, C. (2000). Differential Control of Morning and Evening Components in the Activity Rhythm of Drosophila melanogaster—Sex-Specific Differences Suggest a Different Quality of Activity. J Biol Rhythms *15*, 135–154.

Herrero, A., Duhart, J.M., and Ceriani, M.F. (2017). Neuronal and Glial Clocks Underlying Structural Remodeling of Pacemaker Neurons in Drosophila. Front Physiol *8*, 918.

Jewett, K.A., Thomas, R.E., Phan, C.Q., Lin, B., Milstein, G., Yu, S., Bettcher, L.F., Neto, F.C., Djukovic, D., Raftery, D., et al. (2021). Glucocerebrosidase reduces the spread of protein aggregation in a Drosophila melanogaster model of neurodegeneration by regulating proteins trafficked by extracellular vesicles. PLoS Genet *17*, e1008859.

Jung, W., Liu, C., Yu, Y., Chang, Y., Lien, W., Chao, H., Huang, S., Kuo, C., Ho, H., and Chan, C. (2017). Lipophagy prevents activity-dependent neurodegeneration due to dihydroceramide accumulation in vivo. EMBO Rep *18*, 1150–1165.

Kawasaki, H., Suzuki, T., Ito, K., Takahara, T., Goto-Inoue, N., Setou, M., Sakata, K., and Ishida, N. (2017). Minos-insertion mutant of the Drosophila GBA gene homologue showed abnormal phenotypes of climbing ability, sleep and life span with accumulation of hydroxy-glucocerebroside. Gene *614*, 49–55.

Keatinge, M., Bui, H., Menke, A., Chen, Y.-C., Sokol, A.M., Bai, Q., Ellett, F., Da Costa, M., Burke, D., Gegg, M., et al. (2015). Glucocerebrosidase 1 deficient Danio rerio mirror key pathological aspects of human Gaucher disease and provide evidence of early microglial activation preceding alpha-synuclein-independent neuronal cell death. Hum Mol Genet *24*, 6640–6652.

Kinghorn, K.J., Grönke, S., Castillo-Quan, J.I., Woodling, N.S., Li, L., Sirka, E., Gegg, M., Mills, K., Hardy, J., Bjedov, I., et al. (2016). A Drosophila Model of Neuronopathic Gaucher Disease Demonstrates Lysosomal-

Autophagic Defects and Altered mTOR Signalling and Is Functionally Rescued by Rapamycin. J Neurosci *36*, 11654–11670.

Konopka, R.J., and Benzer, S. (1971). Clock Mutants of Drosophila melanogaster. PNAS *68*, 2112–2116.

Kremer, M.C., Jung, C., Batelli, S., Rubin, G.M., and Gaul, U. (2017). The glia of the adult *Drosophila* nervous system: Glia Anatomy in Adult Drosophila Nervous System. Glia *65*, 606–638.

Krohn, L., Ruskey, J.A., Rudakou, U., Leveille, E., Asayesh, F., Hu, M.T.M., Arnulf, I., Dauvilliers, Y., Högl, B., Stefani, A., et al. (2020). GBA variants in REM sleep behavior disorder: A multicenter study. Neurology *95*, e1008–e1016.

Krzeptowski, W., Hess, G., and Pyza, E. (2018). Circadian Plasticity in the Brain of Insects and Rodents. Frontiers in Neural Circuits *12*, 32.

Kunduri, G., Turner-Evans, D., Konya, Y., Izumi, Y., Nagashima, K., Lockett, S., Holthuis, J., Bamba, T., Acharya, U., and Acharya, J.K. (2018). Defective cortex glia plasma membrane structure underlies light-induced epilepsy in cpes mutants. Proc Natl Acad Sci U S A *115*, E8919–E8928.

Lee, P.-T., Zirin, J., Kanca, O., Lin, W.-W., Schulze, K.L., Li-Kroeger, D., Tao, R., Devereaux, C., Hu, Y., Chung, V., et al. (2018). A gene-specific T2A-GAL4 library for Drosophila. ELife *7*, e35574.

Leng, Y., Musiek, E.S., Hu, K., Cappuccio, F.P., and Yaffe, K. (2019). Association between circadian rhythms and neurodegenerative diseases. Lancet Neurol *18*, 307–318.

Liddelow, S.A., Guttenplan, K.A., Clarke, L.E., Bennett, F.C., Bohlen, C.J., Schirmer, L., Bennett, M.L., Münch, A.E., Chung, W.-S., Peterson, T.C., et al. (2017). Neurotoxic reactive astrocytes are induced by activated microglia. Nature *541*, 481–487.

Lin, G., Lee, P.-T., Chen, K., Mao, D., Tan, K.L., Zuo, Z., Lin, W.-W., Wang, L., and Bellen, H.J. (2018). Phospholipase PLA2G6, a Parkinsonism-Associated Gene, Affects Vps26 and Vps35, Retromer Function, and Ceramide Levels, Similar to α-Synuclein Gain. Cell Metabolism *28*, 605-618.e6.

Lin, G., Wang, L., Marcogliese, P.C., and Bellen, H.J. (2019). Sphingolipids in the Pathogenesis of Parkinson's Disease and Parkinsonism. Trends in Endocrinology & Metabolism *30*, 106–117.

Liu, G., Boot, B., Locascio, J.J., Jansen, I.E., Winder-Rhodes, S., Eberly, S., Elbaz, A., Brice, A., Ravina, B., van Hilten, J.J., et al. (2016). Specifically neuropathic Gaucher's mutations accelerate cognitive decline in Parkinson's. Ann Neurol *80*, 674–685.

Liu, H., Wang, X., Chen, L., Chen, L., Tsirka, S.E., Ge, S., and Xiong, Q. (2021). Microglia modulate stable wakefulness via the thalamic reticular nucleus in mice. Nat Commun *12*, 4646.

Liu, L., Zhang, K., Sandoval, H., Yamamoto, S., Jaiswal, M., Sanz, E., Li, Z., Hui, J., Graham, B.H., Quintana, A., et al. (2015). Glial lipid droplets and ROS induced by mitochondrial defects promote neurodegeneration. Cell *160*, 177–190.

Mazzulli, J.R., Xu, Y.-H., Sun, Y., Knight, A.L., McLean, P.J., Caldwell, G.A., Sidransky, E., Grabowski, G.A., and Krainc, D. (2011). Gaucher Disease Glucocerebrosidase and α-Synuclein Form a Bidirectional Pathogenic Loop in Synucleinopathies. Cell *146*, 37–52.

Meivar-Levy, I., Sabanay, H., Bershadsky, A.D., and Futerman, A.H. (1997). The Role of Sphingolipids in the Maintenance of Fibroblast Morphology: THE INHIBITION OF PROTRUSIONAL ACTIVITY, CELL SPREADING, AND CYTOKINESIS INDUCED BY FUMONISIN B1 CAN BE REVERSED BY GANGLIOSIDE GM3*. Journal of Biological Chemistry *272*, 1558–1564.

Merrill, A.H. (2011). Sphingolipid and Glycosphingolipid Metabolic Pathways in the Era of Sphingolipidomics. Chem Rev *111*, 6387–6422.

Mikulka, C.R., Dearborn, J.T., Benitez, B.A., Strickland, A., Liu, L., Milbrandt, J., and Sands, M.S. (2020). Cell-autonomous expression of the acid hydrolase galactocerebrosidase. Proc Natl Acad Sci USA *117*, 9032–9041.

Musashe, D.T., Purice, M.D., Speese, S.D., Doherty, J., and Logan, M.A. (2016). Insulin-like Signaling Promotes Glial Phagocytic Clearance of Degenerating Axons through Regulation of Draper. Cell Reports *16*, 1838–1850.

Ng, F.S., and Jackson, F.R. (2015). The ROP vesicle release factor is required in adult Drosophila glia for normal circadian behavior. Front Cell Neurosci *9*, 256.

O'Brien, J.S., and Sampson, E.L. (1965). Lipid composition of the normal human brain: gray matter, white matter, and myelin. J Lipid Res *6*, 537–544.

Osellame, L.D., Rahim, A.A., Hargreaves, I.P., Gegg, M.E., Richard-Londt, A., Brandner, S., Waddington, S.N., Schapira, A.H.V., and Duchen, M.R. (2013). Mitochondria and Quality Control Defects in a Mouse Model of Gaucher Disease—Links to Parkinson's Disease. Cell Metab *17*, 941–953.

Pan, T., Kondo, S., Le, W., and Jankovic, J. (2008). The role of autophagy-lysosome pathway in neurodegeneration associated with Parkinson's disease. Brain *131*, 1969–1978.

Parisky, K.M., Agosto, J., Pulver, S.R., Shang, Y., Kuklin, E., Hodge, J.J.L., Kang, K., Liu, X., Garrity, P.A., Rosbash, M., et al. (2008). PDF Cells Are a GABA-Responsive Wake-Promoting Component of the Drosophila Sleep Circuit. Neuron *60*, 672–682.

Park, J.H., Helfrich-Förster, C., Lee, G., Liu, L., Rosbash, M., and Hall, J.C. (2000). Differential regulation of circadian pacemaker output by separate clock genes in Drosophila. PNAS *97*, 3608–3613.

Petsakou, A., Sapsis, T.P., and Blau, J. (2015). Circadian Rhythms in Rho1 Activity Regulate Neuronal Plasticity and Network Hierarchy. Cell *162*, 823–835.

Pfeiffer, B.D., Jenett, A., Hammonds, A.S., Ngo, T.-T.B., Misra, S., Murphy, C., Scully, A., Carlson, J.W., Wan, K.H., Laverty, T.R., et al. (2008). Tools for neuroanatomy and neurogenetics in Drosophila. PNAS *105*, 9715–9720.

Pyza, E., and Meinertzhagen, I.A. (1999). Daily rhythmic changes of cell size and shape in the first optic neuropil in Drosophila melanogaster. Journal of Neurobiology *40*, 77–88.

Raju, D., Schonauer, S., Hamzeh, H., Flynn, K.C., Bradke, F., Dorp, K. vom, Dörmann, P., Yildiz, Y., Trötschel, C., Poetsch, A., et al. (2015). Accumulation of Glucosylceramide in the Absence of the Beta-Glucosidase GBA2 Alters Cytoskeletal Dynamics. PLOS Genetics *11*, e1005063.

Ross, C.A., and Poirier, M.A. (2004). Protein aggregation and neurodegenerative disease. Nat Med *10*, S10–S17.

Ryzhikov, M., Ehlers, A., Steinberg, D., Xie, W., Oberlander, E., Brown, S., Gilmore, P.E., Townsend, R.R., Lane, W.S., Dolinay, T., et al. (2019). Diurnal Rhythms Spatially and Temporally Organize Autophagy. Cell Reports *26*, 1880-1892.e6.

Schafer, D.P., Lehrman, E.K., Kautzman, A.G., Koyama, R., Mardinly, A.R., Yamasaki, R., Ransohoff, R.M., Greenberg, M.E., Barres, B.A., and Stevens, B. (2012). Microglia Sculpt Postnatal Neural Circuits in an Activity and Complement-Dependent Manner. Neuron *74*, 691–705.

Schöndorf, D.C., Aureli, M., McAllister, F.E., Hindley, C.J., Mayer, F., Schmid, B., Sardi, S.P., Valsecchi, M., Hoffmann, S., Schwarz, L.K., et al. (2014). iPSC-derived neurons from GBA1-associated Parkinson's disease patients show autophagic defects and impaired calcium homeostasis. Nat Commun *5*, 4028.

Sellin, J., Schulze, H., Paradis, M., Gosejacob, D., Papan, C., Shevchenko, A., Psathaki, O.E., Paululat, A., Thielisch, M., Sandhoff, K., et al. (2017). Characterization of Drosophila Saposin-related mutants as a model for lysosomal sphingolipid storage diseases. Dis Model Mech *10*, 737–750.

Sidransky, E., and Lopez, G. (2012). The link between the GBA gene and parkinsonism. Lancet Neurol *11*, 986–998.

Sidransky, E., Nalls, M.A., Aasly, J.O., Aharon-Peretz, J., Annesi, G., Barbosa, E.R., Bar-Shira, A., Berg, D., Bras, J., Brice, A., et al. (2009). Multicenter analysis of glucocerebrosidase mutations in Parkinson's disease. N Engl J Med *361*, 1651–1661.

Sivachenko, A., Li, Y., Abruzzi, K.C., and Rosbash, M. (2013). The transcription factor Mef2 links the Drosophila core clock to Fas2, neuronal morphology, and circadian behavior. Neuron *79*, 281–292.

Stanhope, B.A., Jaggard, J.B., Gratton, M., Brown, E.B., and Keene, A.C. (2020). Sleep Regulates Glial Plasticity and Expression of the Engulfment Receptor Draper Following Neural Injury. Current Biology *30*, 1092-1101.e3.

Suresh, S.N., Verma, V., Sateesh, S., Clement, J.P., and Manjithaya, R. (2018). Neurodegenerative diseases: model organisms, pathology and autophagy. J Genet *97*, 679–701.

Tainton-Heap, L.A.L., Kirszenblat, L.C., Notaras, E.T., Grabowska, M.J., Jeans, R., Feng, K., Shaw, P.J., and van Swinderen, B. (2021). A Paradoxical Kind of Sleep in Drosophila melanogaster. Current Biology *31*, 578-590.e6.

Tsai, J.W., Kostyleva, R., Chen, P.-L., Rivas-Serna, I.M., Clandinin, M.T., Meinertzhagen, I.A., and Clandinin, T.R. (2019). Transcriptional Feedback Links Lipid Synthesis to Synaptic Vesicle Pools in Drosophila Photoreceptors. Neuron *101*, 721-737.e4.

Uemura, N., Koike, M., Ansai, S., Kinoshita, M., Ishikawa-Fujiwara, T., Matsui, H., Naruse, K., Sakamoto, N., Uchiyama, Y., Todo, T., et al. (2015). Viable Neuronopathic Gaucher Disease Model in Medaka (Oryzias latipes) Displays Axonal Accumulation of Alpha-Synuclein. PLoS Genet *11*.

Ulgherait, M., Midoun, A.M., Park, S.J., Gatto, J.A., Tener, S.J., Siewert, J., Klickstein, N., Canman, J.C., Ja, W.W., and Shirasu-Hiza, M. (2021). Circadian autophagy drives iTRF-mediated longevity. Nature *598*, 353–358.

Valadas, J.S., Esposito, G., Vandekerkhove, D., Miskiewicz, K., Deaulmerie, L., Raitano, S., Seibler, P., Klein, C., and Verstreken, P. (2018). ER Lipid Defects in Neuropeptidergic Neurons Impair Sleep Patterns in Parkinson's Disease. Neuron *98*, 1155-1169.e6.

Woeste, M.A., Stern, S., Raju, D.N., Grahn, E., Dittmann, D., Gutbrod, K., Dörmann, P., Hansen, J.N., Schonauer, S., Marx, C.E., et al. (2019). Species-specific differences in nonlysosomal glucosylceramidase GBA2 function underlie locomotor dysfunction arising from loss-of-function mutations. J Biol Chem *294*, 3853–3871.

Xie, L., Kang, H., Xu, Q., Chen, M.J., Liao, Y., Thiyagarajan, M., O'Donnell, J., Christensen, D.J., Nicholson, C., Iliff, J.J., et al. (2013). Sleep Drives Metabolite Clearance from the Adult Brain. Science *342*, 10.1126/science.1241224.

Yadav, R.S., and Tiwari, N.K. (2014). Lipid Integration in Neurodegeneration: An Overview of Alzheimer's Disease. Mol Neurobiol *50*, 168–176.

Yildirim, K., Petri, J., Kottmeier, R., and Klämbt, C. (2019). Drosophila glia: Few cell types and many conserved functions. Glia *67*, 5–26.

Zhang, S.L., Yue, Z., Arnold, D.M., Artiushin, G., and Sehgal, A. (2018). A Circadian Clock in the Blood-Brain Barrier Regulates Xenobiotic Efflux. Cell *173*, 130-139.e10.

Zhang, Y., Chen, K., Sloan, S.A., Bennett, M.L., Scholze, A.R., O'Keeffe, S., Phatnani, H.P., Guarnieri, P., Caneda, C., Ruderisch, N., et al. (2014). An RNA-Sequencing Transcriptome and Splicing Database of Glia, Neurons, and Vascular Cells of the Cerebral Cortex. J. Neurosci. *34*, 11929–11947.

Zhang, Y., Sloan, S.A., Clarke, L.E., Caneda, C., Plaza, C.A., Blumenthal, P.D., Vogel, H., Steinberg, G.K., Edwards, M.S.B., Li, G., et al. (2016). Purification and Characterization of Progenitor and Mature Human Astrocytes Reveals Transcriptional and Functional Differences with Mouse. Neuron *89*, 37–53.

Zuchero, J.B., and Barres, B.A. (2015). Glia in mammalian development and disease. Development *142*, 3805–3809.